



IRAS 09002-4732: A Laboratory for the Formation of Rich Stellar Clusters

Konstantin V. Getman¹ , Eric D. Feigelson^{1,2} , Michael A. Kuhn³ , Patrick S. Broos¹ , and Gordon P. Garmire¹

¹Department of Astronomy & Astrophysics, Pennsylvania State University, 525 Davey Lab, University Park, PA 16802, USA; gkosta@astro.psu.edu

²Center for Exoplanets and Habitable Worlds, Pennsylvania State University, USA

³Department of Astronomy, California Institute of Technology, Pasadena, CA 91125, USA

Received 2019 July 30; revised 2019 October 10; accepted 2019 October 10; published 2019 November 19

Abstract

IRAS 09002-4732 is a poorly studied embedded cluster of stars in the Vela Molecular Ridge at a distance of 1.7 kpc. Deep observations with the *Chandra X-ray Observatory*, combined with existing optical and infrared surveys, produce a catalog of 441 probable pre-main-sequence members of the region. The stellar spatial distribution has two components: most stars reside in a rich, compact, elliptical cluster, but a minority reside within a molecular filament several parsecs long that straddles the cluster. The filament has active distributed star formation with dozens of unclustered protostars. The cluster pre-main-sequence population is ≤ 0.8 Myr old and deeply embedded; its most massive member is extremely young, producing an ultracompact H II region. The cluster total population deduced from the X-ray luminosity function is surprisingly rich, twice that of the Orion Nebula Cluster. The cluster core is remarkably dense where strong N -body interactions should be occurring; its initial mass function may be deficient in massive stars. We infer that IRAS 09002-4732 is a rare case where a rich cluster is forming today in a molecular filament, consistent with astrophysical models of cluster formation in clouds that involve the hierarchical formation and merging of groups in molecular filaments.

Unified Astronomy Thesaurus concepts: [Dense interstellar clouds \(371\)](#); [Collapsing clouds \(267\)](#); [Interstellar filaments \(842\)](#); [Compact H II region \(286\)](#); [Protostars \(1302\)](#); [Infrared excess \(788\)](#); [Single X-ray stars \(1461\)](#); [Young star clusters \(1833\)](#); [Star forming regions \(1565\)](#); [Pre-main sequence \(1289\)](#)

Supporting material: machine-readable tables

1. Introduction

1.1. The Formation of Star Clusters

Most stars in the Galaxy are field stars, but originate in rich clusters within giant molecular cloud complexes (Lada & Lada 2003). The mechanisms by which rich clusters form has not been easy to discern. An understanding is emerging that rich clusters do not form monolithically in a single event of gravitational collapse, but rather are produced hierarchically from the merger of small groups that collapse asynchronously in molecular filaments within cloud complexes. Hydrodynamical calculations of star formation under realistic cloud conditions suggest that this hierarchical cluster formation process extends over millions of years, slowed by turbulence and stellar feedback (Bate et al. 2003; Federrath 2015; Vázquez-Semadeni et al. 2017, 2019). Empirical evidence for this scenario has been accumulating from disparate findings: the ubiquity of turbulence in molecular clouds (Mac Low & Klessen 2004), the prevalence of filamentary molecular structures (André et al. 2010), detection of complicated kinematics in filaments including gravitational infall (Schneider et al. 2010; Zhang et al. 2017), and discovery of spatiotemporal gradients in rich young clusters (Getman et al. 2018a). The latter phenomenon, unexpected from simple cluster formation models, requires continuing star formation in cluster cores.

A clear example of a rich cluster—that is, thousands of stars dominated by massive OB stars—in the solar vicinity that is now forming from infalling and merging filaments has been difficult to find. A young cluster with 1000 members will typically have a star with maximum mass $\sim 40 M_{\odot}$ (Popescu & Hanson 2014.) The Spokes Cluster in the NGC 2264 star-forming region at $d \simeq 0.8$ kpc has over a dozen protostars closely associated with dusty filaments, but the dominant star does not form an H II region; the cluster population is only a few hundred stars and the filaments

are < 1 pc in length (Teixeira et al. 2006; Kuhn et al. 2015b). IC 5146 (=Cocoon Nebula), with $d \simeq 0.8$ kpc, is an embedded cluster with young protostars, dominated by a B0 star with several short (< 1 pc) dusty filaments; however, its total population does not exceed a couple hundreds of stars (Johnstone et al. 2017). Many more ultracompact H II regions tracing current OB star formation are known at distances 3–15 kpc, where the greater distance inhibits detailed study (Wood & Churchwell 1989). Perhaps the most interesting case is W3 Main at $d \simeq 2$ kpc, which is a populous, spherical, embedded cluster with at least ~ 2000 stars and a remarkable concentration of OB stars of different ages in the cluster core (Tieftrunk et al. 1997; Feigelson & Townsley 2008; Broos et al. 2013; Bik et al. 2014). A small molecular filament ($0.5 \times < 0.1$ pc) has been identified among the W3 Main H II regions, and the cluster appears to be fed by several larger dusty filaments several parsecs in length (Tieftrunk et al. 1998; Rivera-Ingraham et al. 2013).

The most detailed observational examination of star formation in massive clouds has been made in the nearby Orion molecular cloud complex at distance $d \simeq 0.4$ kpc (Bally 2008; Rezaei et al. 2018). It shows that the process of large-scale star formation can be very complicated, extending over tens of parsecs and millions of years.

Current active star formation in the filamentary Orion A cloud is concentrated along its head with projected length $\simeq 10$ pc, such that the protostars are distributed in the OMC 2/3 region, and in the small clusters associated with the Becklin-Neugebauer object in OMC-1 (Johnstone & Bally 1999; Grosso et al. 2005; Megeath et al. 2012). The present-day molecular cloud is surrounded by thousands of stars, some associated with distinct OB associations and others that have probably drifted from the current star-forming filament (Blaauw 1991; Carpenter et al. 2001; Bouy et al. 2014;

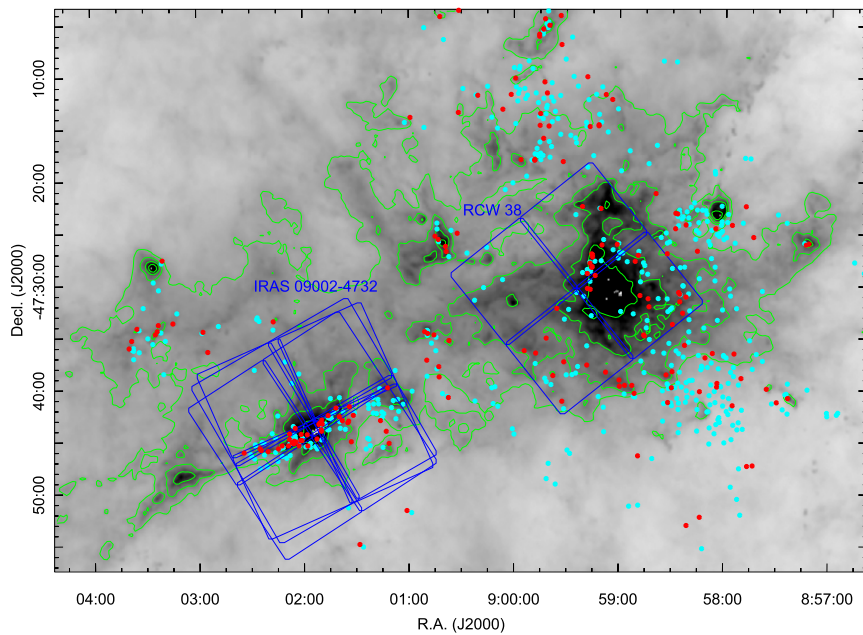


Figure 1. A $1^{\circ}3 \times 0^{\circ}9$ (39×27 pc at a distance of 1.7 kpc) dust map from the $250 \mu\text{m}$ band *Herschel* SPIRE instrument, showing the IRAS 09002-4732 and RCW 38 star-forming regions and their environs. Green contours show levels of infrared surface brightness. Circles show *Spitzer*-selected infrared-excess stars. Red indicates Stage 1, corresponding to Class 0/I protostars. Cyan indicates Stage 2, corresponding to Class II/III pre-main-sequence stars (Povich et al. 2013). Blue polygons show the MYSIX and IRAS 09002-4732 *Chandra* fields.

Kounkel et al. 2018). Dozens of supernova explosions have produced hot bubbles spanning >100 pc (Bally 2008). Smaller clusters formed a few million years ago are still present as coherent structures with proper motions reflecting the motions of cloud components that are now partially or completely dissipated (Getman et al. 2019).

The most prominent structure is the Orion Nebula Cluster (ONC), a compact rich cluster of several thousand stars, mostly 1–3 Myr old, with a dense central concentration of higher-mass stars known as the Trapezium (Hillenbrand 1997; O’Dell 2001). However, the molecular cloud structure giving rise to the ONC is now dissipated, so the formation process of the ONC is uncertain.

1.2. IRAS 09002-4732: A Laboratory for Rich Cluster Formation

We discuss here IRAS 09002-4732, a young stellar cluster that resembles the ONC (both are associated with a molecular filament several parsecs long) but at an earlier stage of evolution. The principal infrared and molecular studies of the region are by Lenzen (1991) and Apai et al. (2005). Located in the Vela Molecular Ridge (VMR-A), the stellar population is concentrated in a cluster still embedded in—and likely destroying—its natal cloud. Its dominant star has a spectral type around O7, similar to $\theta^1\text{C Ori}$ in the ONC. However, it is heavily obscured, with $A_V \simeq 20$ mag, producing a cometary ultracompact H II region $\simeq 0.05$ pc in extent. In contrast, $\theta^1\text{C Ori}$ and its nearby Trapezium stars are unobscured and produce a giant H II region >2 pc in extent. In both cases, the dominant star is projected close to dense molecular cores (Lapinov et al. 1998), although in the ONC case, the star cluster lies in the foreground evacuated H II region. The molecular properties and massive stellar product of the nearby VMR-C molecular region are also similar to those of the Orion A cloud (Yamaguchi et al. 1999).

In this study, we show that the analogy between the ONC and IRAS 09002-4732 is strong by improving the stellar census of the

IRAS 09002-4732 cloud, comparing its properties to other nearby rich young clusters, and demonstrating that it lies within a molecular filament populated by many protostars. Our group encountered this active star formation in the larger elongated structure while constructing the MYSIX Infrared-Excess Source (MIRES; Povich et al. 2013) catalog members associated with the nearby RCW 38 rich cluster. Figure 1 shows a wide area of the infrared sky encompassing the RCW 38 and IRAS 09002-4732 regions, with MIRIS-selected stars superimposed.

Our follow-up study found a rich group of 24 candidate Class 0/I protostars in the region $09^{\text{h}}01^{\text{m}}12^{\text{s}} < \alpha < 09^{\text{h}}02^{\text{m}}24^{\text{s}}$ and $-47:40 < \delta < -47:45$ (Romine et al. 2016). They lie along a dusty filament, seen in *Herschel* infrared maps, that is oriented northwest to southeast and bifurcated by the older IRAS 09002-4732 star cluster. Romine et al. selected the protostars based on UKIDSS *JHK* and *Spitzer* 3.6–8.0 μm spectral energy distributions; several also exhibit a 4.5 μm excess characteristic of shocked molecular protostellar outflows (Cyganowski et al. 2008). These photometrically selected protostars have a wide range of luminosities, with 8 μm brightnesses ranging from 5 to 12 mag. Some are quite massive protostars, but the brightest is two orders of magnitude less luminous than the dominant O7 star of the IRAS 09002-4732 cluster (Appendix A).

Povich et al. (2013) and Romine et al. (2016) thus found active star formation in a molecular filament around the somewhat older (and much richer) IRAS 09002-4732 star cluster, all of which appears younger than that of the ONC. This motivates further study to characterize the IRAS 09002-4732 region more completely, compare it to other nearby young clusters, and investigate whether empirical insights can emerge regarding the birth of ONC-type rich clusters.

1.3. The Role of X-Ray Imaging

Our observational effort here starts with an improvement in the stellar census of IRAS 09002-4732, both in its central cluster

and distributed in the surrounding molecular material. This is achieved with deep exposures using NASA’s *Chandra X-ray Observatory*, together with complementary infrared surveys. *Chandra* effectively detects rich pre-main-sequence (PMS) populations in star-forming regions, out to several kiloparsecs in the Galactic Plane, primarily due to enhanced magnetic dynamos and subsequent magnetic reconnection flaring in fully convective rapidly rotating stars; see reviews by Güdel (2007) and Feigelson (2018). Solar-mass PMS stars are typically 10^2 – 10^3 times more X-ray luminous than the contemporary Sun, and can thus be readily differentiated from most main-sequence field stars by virtue of elevated X-ray emission. The flare X-ray spectrum is harder than typically seen in solar flares, so PMS stars can often be detected even if embedded in their natal cloud.

Our group has produced catalogs of >40,000 PMS stars with X-ray and infrared surveys in $\simeq 40$ OB-dominated clusters in massive star-forming complexes out to distances $\simeq 3$ kpc (Getman et al. 2005, 2017; Townsley et al. 2011b; Broos et al. 2013; Feigelson et al. 2013). In addition to providing an improved census of PMS members of a star-forming region, the X-ray photometry and spectra, together with near-infrared photometry, allow estimates of individual stellar masses, ages, and line-of-sight absorptions (Getman et al. 2010, 2014). We also use X-ray properties as measures of the spatial structure and total population of the PMS populations (Kuhn et al. 2014, 2015b). With this multifaceted characterization of the stellar population produced in a molecular cloud over millions of years, new empirically based insights into the cluster formation process can be sought. Recent results from some of these X-ray studies have been reviewed by Feigelson (2018).

The X-ray observations of IRAS 09002-4732, together with methods of data reduction and inference of astronomical properties, are described in Section 2. The results of *Chandra* X-ray imaging and catalog of probable cloud members are presented in Section 3. Inference of stellar and cluster properties—such as initial mass function (IMF), total population, age, spatial structure, and stellar densities—are developed in Section 4. The final section (Section 5) discusses the star formation history of the region, as well as its role as a young analog of the ONC region. Appendices provide details on the stars in the core of the IRAS 09002-4732 cluster and stellar ages in the nearby rich RCW 38 cluster.

2. Data and Analysis

Three observations of IRAS 09002-4732 were obtained during *Chandra X-ray Observatory* Cycle 18 using the Advanced CCD Imaging Spectrometer imaging array (ACIS-I; Garmire et al. 2003). The $17' \times 17'$ image from four contiguous CCD chips was centered at $(\alpha, \delta)_{J2000} = (09:01:55.00, -47:43:46.8)$ and the total exposure was close to 100 ks. The instrument was operated in Very Faint Timed Exposure mode. Exposure details are provided in Table 1. Data quality is excellent.

Data analysis closely followed procedures from our earlier projects studying PMS populations (references above), and is briefly summarized here. The suite of *ACIS Extract* procedures described by Broos et al. (2010) provides very sensitive and reliable identification of faint X-ray sources in *Chandra* images.⁴

⁴ Some more elaborate methods used in some of our previous studies—such as probabilistic matching to infrared catalogs (Naylor et al. 2013), parametric modeling of field star and extragalactic contaminant populations, and naive Bayes classification to reduce contamination (Broos et al. 2013)—were not applied here.

Table 1
Chandra Exposures

ObsID	Type ^a	Date	Exp ^b (ks)
18891	GO	2017-03-03	49.3
19710	GTO	2017-09-04	28.3
20727	GTO	2017-09-09	21.8

Notes.

^a GO = Guest Observer; GTO = Guaranteed Time Observation, *Chandra* ACIS Team.

^b Exposure times are the net usable times after removal of high instrumental background.

1. A deep catalog of candidate sources is obtained from bumps in a smoothed map of the field based on maximum likelihood deconvolution using the known spatially variable instrument point-spread function (PSF). Local background levels are iteratively calculated for each candidate source; this is necessary because the three exposures have misaligned roll angles and chip gaps. This candidate source identification procedure is performed on the merged image from the three exposures in Table 1.
2. A global astrometric correction to the pointing direction is made by removing any offset between bright X-ray sources and 2MASS counterparts. This allows subarcsecond positional accuracy for on-axis sources.
3. Photons are extracted for each candidate source in small regions scaled to the local point-spread function, typically containing 90% of the expected photons. Local background rates are identified and subtracted to give net source counts. The local exposure time is obtained from the merged exposure map.
4. A variety of X-ray properties are then calculated from the extracted events: net count rate corrected for local exposure time and point-spread function tails; source locations with errors depending on off-axis angle and net count rate; probability of source existence based on Poisson distributions for the source and background photon rates; hypothesis tests for variability in the photon arrival times using a Kolmogorov–Smirnov test; and median energy of the net counts.
5. Line-of-sight interstellar extinction to the source is obtained from the median photon energy, and an absorption-corrected X-ray luminosity is obtained for each source. These calculations, based on the *XPHOT* method described by Getman et al. (2010), are restricted to sources with >5–7 net counts.

3. PMS Members of IRAS 09002-4732

3.1. X-Ray Sources and Stellar Counterparts

Table 2 lists the 1034 candidate X-ray sources in the IRAS 09002-4732 region obtained using the procedures outlined in Section 2. This candidate X-ray source list is purposefully very sensitive and contains spurious noise features. They are kept here because, in our experience, some of the weaker candidates have clear infrared candidates and are likely PMS members of the region. Spurious noise features and real X-ray sources associated with background extragalactic objects will rarely have optical and infrared (OIR) counterparts.

Table 2
Candidate X-Ray Sources

CXOU J	Position				Extraction					Characteristics		
	α J2000	δ	Error "	θ '	C_{net} counts	σ_{net} counts	B counts	PSF Frac	$\log P_B$	Anom	Var	ME (keV)
090106.38–474137.6	135.276618	–47.693802	1.26	8.0	4.8	3.0	4.2	0.90	–2.9	2.9
090106.52–474429.7	135.277185	–47.741607	0.69	8.2	30.3	6.4	9.7	0.90	<–5	...	2	2.6
090107.22–473954.1	135.280123	–47.665039	2.26	8.5	1.6	1.7	1.4	0.61	–1.1	g	...	1.5
090107.84–474057.9	135.282690	–47.682762	1.10	8.0	4.8	2.5	1.2	0.56	–2.9	...	1	1.7
090109.07–474108.4	135.287798	–47.685693	1.16	8.1	6.6	3.9	8.4	0.90	–2.2	g	...	5.4
090109.31–474708.3	135.288823	–47.785649	1.93	8.4	2.3	2.8	10.7	0.90	–0.9	3.9
090109.56–474426.0	135.289860	–47.740581	0.96	7.7	9.4	4.2	7.6	0.90	–4.0	...	1	2.1
090109.84–474149.0	135.291008	–47.696972	0.56	7.8	28.5	6.2	8.5	0.90	<–5	2.3
090144.19–474000.9	135.434129	–47.666930	0.06	4.2	287.8	17.1	1.2	0.90	<–5	...	2	1.3
090146.08–474957.9	135.442019	–47.832768	0.15	6.4	191.8	14.1	4.2	0.90	<–5	...	2	2.6
090154.63–474411.1	135.477666	–47.736417	0.19	0.6	5.2	2.5	0.8	0.90	–3.8	g	...	5.0
090201.21–474455.9	135.505080	–47.748875	0.27	1.6	2.8	1.8	0.2	0.90	–4.1	g	...	3.1
090153.81–474415.7	135.474218	–47.737710	0.10	0.6	17.6	4.3	0.4	0.91	<–5	ga	...	2.3
090154.10–474412.1	135.475448	–47.736718	0.20	0.6	4.3	2.3	0.7	0.90	–2.8	g	...	4.0
090154.11–474410.3	135.475484	–47.736197	0.10	0.5	19.9	4.6	1.1	0.90	<–5	g	...	3.1
090154.29–474408.8	135.476224	–47.735789	0.11	0.5	5.8	2.9	2.2	0.55	–2.8	g	...	4.8
090154.33–474410.3	135.476415	–47.736201	0.03	0.5	111.1	10.7	1.9	0.75	<–5	g	...	3.8
090154.36–474408.5	135.476522	–47.735720	0.10	0.5	6.9	2.9	1.1	0.57	–4.5	g	...	4.1
090154.38–474409.5	135.476588	–47.735981	0.09	0.5	4.3	2.7	2.7	0.42	–3.8	g	...	5.1
090154.63–474411.1	135.477666	–47.736417	0.19	0.6	5.2	2.5	0.8	0.90	–3.8	g	...	5.0
090154.75–474421.6	135.478157	–47.739350	0.23	0.7	2.7	1.8	0.3	0.86	–2.5	g	...	3.9
090154.78–474407.7	135.478276	–47.735498	0.21	0.5	3.6	2.1	0.4	0.83	–3.4	3.5
090154.89–474406.7	135.478713	–47.735210	0.23	0.5	2.6	1.8	0.4	0.81	–2.3	5.4
090155.32–474412.9	135.480536	–47.736937	0.26	0.6	2.6	1.8	0.4	0.91	–2.2	g	...	4.2

Note. Column definitions are as follows. CXOU: *Chandra X-ray Observatory* Unidentified source. α , δ , Err: Right ascension and decl. (in decimal degrees) for epoch J2000.0, with the 63% error circle representing the random component of position uncertainty. The field is astrometrically aligned to the 2MASS reference frame. θ : Off-axis angle (in arc minutes) from the pointing direction of the ACIS imager. The mirror point spread functions deteriorates nonlinearly as θ increases. C_{net} , σ_{net} , B , PSF Frac, $\log P_B$: Counts extracted in the PSF-shaped polygon for source characterization in the 0.5–8 keV band. The total number of extracted counts is $C_{\text{net}} + B$, where B is the local background counts scaled to the extraction area and C_{net} is the net source counts after background subtraction. PSF Frac is the fraction of the local point-spread function captured in the extraction polygon. A reduced PSF fraction (significantly below 90%) may indicate that the source is in a crowded region. Here, $\log P_B$ is the logarithm of the probability that the source is spurious (specifically, that the observed total number of extracted counts will occur in a single trial of the Poisson distribution given the observed background counts B). Anom: Anomaly flag. Flag “a” reports that photometry and spectrum may contain >10% cosmic ray afterglow events in the detector. Flag “g” reports that the source spent more than 10% of the observation on dead regions of the detector (principally chip gaps). Var: Variability flag based on the Kolmogorov–Smirnov test. An ellipse “...” indicates no evidence of variability. The number “1” indicates possible ($0.005 < P_{\text{KS}} < 0.05$) variability. The number “2” indicates very probable variability ($P_{\text{KS}} < 0.005$). Variability can be present within a single *Chandra* exposure, in the merged *Chandra* exposures, or between averaged *Chandra* exposures. Spurious indications can be produced by satellite dithering across dead regions of the detector, or by variations in the background rather than source photon arrival rate. ME: Median energy (in keV) of the background-subtracted photons.

(This table is available in its entirety in machine-readable form.)

Omitting the handful of X-ray candidates with <2.0 net counts, this X-ray catalog was matched to four OIR catalogs of point sources⁵: VPHAS+–DR2, *Gaia*–DR2 in a broad optical band, 2MASS in the *JHK* near-infrared bands, and *Spitzer* IRAC in four mid-infrared bands in the range 3.6–8.0 μm . In addition, we checked the 264 *JHK* stars listed by Apai et al. (2005) in the inner region of IRAS 09002–4732.

The search radius for finding counterparts from X-ray centroids (Table 2) was chosen to be 1'' within the central part of the ACIS field, and 2'' for off-axis angles exceeding 4'. Among 1034 X-ray candidate sources, 166, 110, 244, and 201

have matches with sources from the VPHAS+, *Gaia*, 2MASS, and IRAC catalogs, respectively. Taking duplicates into account, 300 of the X-ray candidate sources have OIR counterparts. We have confirmed that the celestial positions of the X-ray sources and 2MASS sources are well-aligned, with no measurable (<0.''1) systematic offset.

An additional 86 X-ray sources without OIR counterparts are spatially clustered in the central part of the region. The combined sample of the 300 and 86 X-ray sources is given in Table 3. Table 4 gives a further subsample of 55 non-X-ray disk-bearing stars from Povich et al. located within the *Chandra* field. These two subsamples are described later in this section.

The total sample of 441 (300 + 86 + 55) young stellar candidates are then subject to three stages of statistical analysis. First, their spatial distribution is segmented into the sum of ellipsoidal isothermal spheres plus a uniform background population, following the methodology of Kuhn et al. (2014) and Kuhn & Feigelson (2019). This is performed with a maximum likelihood mixture model where the optimal number

⁵ Three catalogs were accessed from the online Vizier catalog service provided by the University of Strasbourg Centre des Données Stellaires (CDS) as follows: the VST Photometric H α Survey of the Southern Milky Way and Bulge (VPHAS+) at <http://cdsarc.u-strasbg.fr/viz-bin/Cat?II/341>, *Gaia* Data Release 2 (DR2) at <https://vizier.u-strasbg.fr/viz-bin/VizieR-3?-source=1/345/gaia2>, and the Two Micron All-Sky Survey (2MASS) at <http://vizier.u-strasbg.fr/cgi-bin/VizieR?-source=B/2mass>. The *Spitzer* IRAC source catalog was obtained from the electronic edition of the MYSIX Infrared-Excess Source (MIREs) by Povich et al. (2013).

of ellipsoids is obtained using the penalized likelihood Akaike Information Criterion. Second, the total population of each cluster is estimated by scaling the truncated X-ray Luminosity Function (XLF) to the more complete XLF of the ONC, as described by Kuhn et al. (2015b). Third, the age of each stellar cluster is estimated in two fashions: the Age_{JX} chronometer for PMS stars that uses absorption-corrected X-ray luminosities and J magnitudes (Getman et al. 2014), and the traditional Age_r chronometer based on the optical color–magnitude diagram.

Some caveats regarding the completeness and reliability of this catalog of X-ray selected sources are needed:

1. All OIR catalogs in the central region of IRAS 09002-4732 are subject to spatially variable nebulosity from the H II region and dense dusty molecular filaments (Apai et al. 2005). This gives patchy catalog coverage even from uniform OIR surveys such as VPHAS+, 2MASS, and UKIDSS. These problems are evidenced in the low-quality detections or nebular contamination reported in 2MASS quality flags. More complete OIR coverage would give additional counterparts to the candidate X-ray sources.⁶
2. In the X-ray band, the central 10''–15'' of the cluster suffers reduced exposure due to the 11'' physical gaps between the CCDs of the ACIS-I array. These are shown in the blue outlines of the chips in Figure 1. This is partially overcome by the 16'' Lissajous-shaped dithering pattern of the satellite aspect system (Chandra X-ray 2018). For the sum of the three observations in Table 1, the resulting effective exposure in the inner few arcseconds of the cluster is roughly half that of the rest of the region, resulting in a localized deficit of sources in the innermost cluster core.
3. Random Galactic field stars or extragalactic sources can lie within 1''–2'' radii of X-ray sources. Based on simulations of contaminant populations for the MYStIX *Chandra* observation of the nearby RCW 38 cluster, ~200 of the 1034 candidate X-ray sources (Table 2) are likely true X-ray sources unrelated to the IRAS 09002-4732 star-forming region (Broos et al. 2013). However, the majority are quasars extremely faint in the OIR bands (particularly after extinction by cloud material) and will not appear in our list of likely PMS members. Following the SFiNCs analysis of Getman et al. (2017) involving shifts of the ACIS field in different directions, we estimate that ~8% of the OIR counterparts are stellar contaminants, consistent with the simulations of Broos et al.

Fifty-five infrared sources, undetected in X-rays, lie within the *Chandra* IRAS 09002-4732 field, typically having seven bands of photometry from 2MASS and *Spitzer* IRAC. These were identified in the MIREs catalog of Povich et al. (2013) as sources with spectral energy distributions indicative of disk-

bearing PMS stars, and are listed in Table 4. The criteria selecting these objects from the vast majority of older stars in the infrared catalogs are stricter than those usually applied in studies of nearby young stellar object populations, to reduce contamination by the many dusty red giants that contaminate deep infrared surveys in the Galactic Plane. Twenty-one of these sources have infrared spectral energy distributions characteristic of protostars, denoted Stage 1 by Povich et al. The MIREs protostars in the vicinity of IRAS 09002-4732 have a distribution of 2–8 μm luminosities similar to that of the typical protostars in the Orion cloud, but this distribution is missing the high-luminosity tail seen in Orion (Megeath et al. 2012).

Figure 2 is an “X-ray color–magnitude diagram” that provides information about the reliability of the 1034 X-ray candidate sources. The red and green symbols show sources with ≥ 4 net counts in the ACIS image—which, in most cases, is a statistically significant X-ray source. From experience with X-ray color–magnitude diagrams from the MYStIX and SFiNCs surveys (Broos et al. 2013; Kuhn et al. 2013; Getman et al. 2017), we expect the sources shown in red with OIR counterparts to be PMS members of the region. The green hard-spectrum sources without OIR counterparts are composed of both contaminant populations (extragalactic and Galactic) and PMS stars; in the latter case, the stars are missing from the OIR catalogs due to H II region nebulosity and/or heavy cloud extinction. Note that PMS stars with X-ray median energies ranging from 2.5 to 5 keV will have K band extinctions ranging from ~1 to ~10 mag (Getman et al. 2010.) Among the sources with 2–4 net counts, the majority of cyan ones are likely PMS stars, while the yellow ones are either spurious noise fluctuations from the X-ray image or contaminant populations. From this analysis, we conclude that the X-ray membership sample is likely to include several spurious sources (cyan symbols) and miss some real members (green symbols). These deficiencies can be alleviated if deeper X-ray and high-resolution infrared images of the 17' \times 17' region are obtained.

The spatial distribution of all X-ray sources detected in the IRAS 09002-4732 field is shown in Figure 3, superposed on a 250 μm map of the cool dust from the *Herschel*-SPIRE instrument. The four panels show subsamples using the same color scheme as in Figure 2. The left panels show X-ray candidate sources with OIR counterparts, while the right panels show sources without counterparts. The upper left panel shows the reliable subsample of stronger X-ray sources (>4 net counts) with OIR counterparts, including sources both concentrated toward the center of the rich cluster and distributed widely around the molecular cloud. The lower left panel shows that tentative X-ray sources with OIR counterparts (cyan) have a similar spatial distribution, suggesting they are mostly real members.

The candidate X-ray sources without OIR counterparts are shown in the right panels of Figure 3: the top panel has sources with >4 net counts, and the lower panel has sources with 2–4 net counts. Two distinctive spatial groups are present: several dozen X-ray sources are densely concentrated in the cluster core, while most are scattered uniformly across the ACIS field. A random distribution is expected from background quasars or spurious noise sources. The concentrated group most likely reveals true members of the PMS cluster despite the absence of OIR counterparts or high statistical significance in the X-ray image. We find a concentration of 86 X-ray sources without

⁶ An example of this effect is that six additional candidate X-ray sources have counterparts within 1'' in the list of 268 *JHK* sources from high-resolution VLT/ISAAC images presented by Apai et al. (2005), available from the Vizier database at <http://vizier.u-strasbg.fr/viz-bin/VizieR?source=J/A+A/434/987>. These sources are: (ISAAC Seq #, CXOU) = (306, 090145.23–474513.6), (533, 090156.03–474512.2), (544, 090156.69–474535.7), (560, 090157.32–474542.4), (632, 090201.43–474537.5), (652, 090202.45–474525.1). These stars have $K \sim 13$ –15 mag and are absent from the 2MASS catalog due to the confusing nebulosity and absorption of the region discussed by Apai et al. We do not include these sources in our analysis, as this infrared catalog is incomplete in flux and spatial coverage.

Table 3
X-Ray PMS Members of IRAS 09002-4732

Seq	CXOU	$\log L_x$ (erg s^{-1})	$\log N_H$ (cm^{-2})	2MASS	J (mag)	H (mag)	K (mag)	Qual	IRX	Age _{JX} (Myr)
1	090105.86-474209.1	30.41 ± 0.37	22.25 ± 0.30	09010578-4742103	16.34 ± 0.11	14.70 ± 0.05	13.76 ± 0.05	BAA000	-0.04	...
2	090106.52-474429.7	30.92 ± 0.21	22.36 ± 0.14	09010653-4744298	16.68 ± 0.14	15.42 ± 0.11	14.99 ± 0.13	CAB000	-0.34	...
3	090107.40-474101.2	30.72 ± 0.32	22.23 ± 0.37	09010749-4741014	$17.73 \pm \dots$	15.76 ± 0.16	14.37 ± 0.10	UCA000	0.22	...
4	090109.07-474108.4	31.49 ± 0.70	23.60 ± 0.34
5	090109.56-474426.0	30.29 ± 0.37	22.23 ± 0.30	09010955-4744261	16.91 ± 0.20	15.81 ± 0.14	15.12 ± 0.16	CBC000	0.02	...
Ch1	Ch2	Ch3	Ch4	α_{SED}	r (mag)	i (mag)	$A_V(JHK)$ (mag)	Age _{ri} (Myr)	Plx (mas)	
12.82 ± 0.05	12.45 ± 0.10	12.03 ± 0.14	11.48 ± 0.10	-1.31	
...	20.81 ± 0.09	
13.18 ± 0.06	12.77 ± 0.07	12.33 ± 0.11	12.07 ± 0.18	-1.42	
14.32 ± 0.06	13.40 ± 0.09	12.56 ± 0.16	11.85 ± 0.09	0.03	
14.44 ± 0.10	14.08 ± 0.15	-1.49	...	20.96 ± 0.07	

Note. Column definitions are as follows. Seq: Sequence number of X-ray selected probable members of IRAS 09002-4732. CXOU: *Chandra X-ray Observatory* Unidentified source. $\log L_x$: log X-ray luminosity of sources (assuming distance of 1.7 kpc) obtained with XPHOT (Getman et al. 2010). $\log N_H$: log hydrogen column density along the line-of-sight from the median energy of extracted photons obtained with XPHOT. 2MASS, J , H , K , $Qual$: 2MASS catalog identifier, JHK magnitudes, and quality flags. IRX: Infrared excess derived from 2MASS color-color and color-magnitude diagrams. Age_{JX}: Stellar age estimated from 2MASS and *Chandra* magnitudes as described by Getman et al. (2017). Ch1, Ch2, Ch3, Ch4: *Spitzer* IRAC magnitudes in Channels 1 (3.5 μm), 2 (4.5 μm), 3 (5.6 μm), and 4 (8.0 μm) bands. α_{SED} : Apparent infrared spectral energy distribution slope derived from IRAC photometry. i , r : VPHAS+ r and i band magnitudes. $A_V(JHK)$: Visual absorption estimated from 2MASS JHK colors. Age_{ri}: Stellar age estimated from VPHAS+ $r - i$ color-magnitude diagram. Plx: *Gaia* parallax.

(This table is available in its entirety in machine-readable form.)

Table 4
MIRES Sources from Povich et al. (2013) Undetected in X-Rays

Seq	IRAC	R.A.	Decl.	J	H	K	Ch1	Ch 2	Ch 3	Ch 4	α_{SED}	α_N	Stage
387	G268.2943-00.9270	135.26	-47.69	...	15.00 ± 0.07	13.43 ± 0.05	11.88 ± 0.05	11.16 ± 0.05	10.74 ± 0.10	10.11 ± 0.10	-0.77 ± 0.12	4	-1
388	G268.2940-00.9156	135.28	-47.68	13.85 ± 0.06	13.22 ± 0.09	12.56 ± 0.15	11.45 ± 0.17	-0.19 ± 0.18	4	-1
399	G268.3193-00.9338	135.28	-47.71	16.62 ± 0.14	15.04 ± 0.06	14.32 ± 0.07	13.19 ± 0.07	12.74 ± 0.09	12.13 ± 0.16	11.27 ± 0.18	-0.71 ± 0.20	4	-1
400	G268.2619-00.8819	135.28	-47.64	14.13 ± 0.05	12.73 ± 0.05	11.61 ± 0.05	10.22 ± 0.05	9.83 ± 0.05	9.28 ± 0.10	8.47 ± 0.10	-0.89 ± 0.12	4	2
401	G268.3562-00.9516	135.30	-47.75	...	15.77 ± 0.14	14.88 ± 0.12	13.45 ± 0.07	12.04 ± 0.05	10.73 ± 0.10	9.96 ± 0.10	1.30 ± 0.14	4	1

Note. Information in this table is from Povich et al. (2013), except for α_{SED} , the infrared spectral slope calculated from α_N photometric IRAC points. Stage = 1 corresponds to a Class 0/I protostar; Stage = 2 corresponds to a Class II/III PMS star; Stage = -1 corresponds to an ambiguous status. These sources are not detected in the *Chandra* field.

(This table is available in its entirety in machine-readable form.)

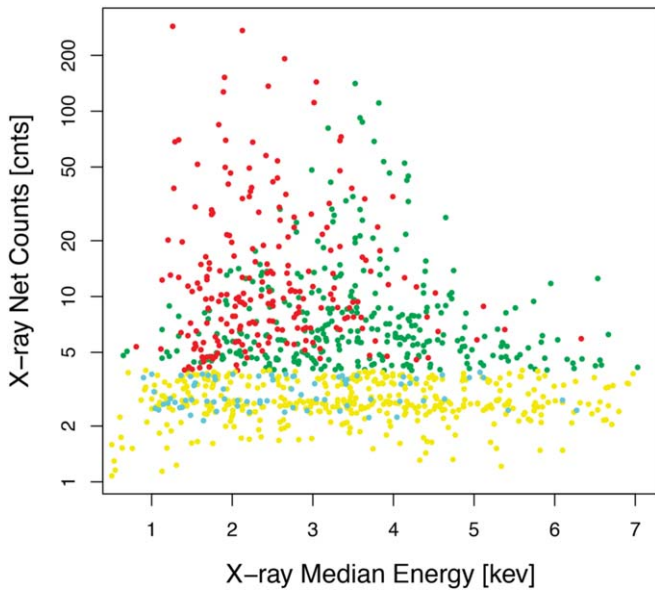


Figure 2. Sample of 1034 candidate X-ray sources in the IRAS 09002-4732 *Chandra* field with three properties: net counts C_{net} in the 0.5–8 keV band, median energy ME (in keV) of the net counts, and existence of OIR counterparts. Candidate sources with counterparts are plotted in red if $C_{\text{net}} > 4$, and in cyan if $2 < C_{\text{net}} < 4$. Candidate sources without counterparts are plotted in green if $C_{\text{net}} > 4$, and in yellow if $C_{\text{net}} < 4$.

OIR counterparts projected within a chosen radius $1/5$ of a central location at $(\alpha, \delta) = (135^{\circ}47435, -47^{\circ}72820)$. This corresponds to a cluster with diameter 1.5 pc; this encompasses the molecular cores, infrared reflection nebosity, and many of the infrared-excess stars identified by Apai et al. (2005).

3.2. The IRAS 09002-4732 Member Sample

For the present study, we construct a sample of 441 probable stellar “members” of the IRAS 09002-4732 region as the union of three subsamples:

1. Three hundred candidate X-ray sources with >2 X-ray net counts that have a counterpart within $1''$ – $2''$ in any of the four OIR catalogs, listed in Table 3;
2. Eighty-six candidate X-ray sources with >2 X-ray net counts that lie projected against the central part of the cluster (a circle with diameter 1.5 pc) and lack an OIR counterpart, also listed in Table 3;
3. Fifty-five members of the MIREs catalog with infrared excesses located within the *Chandra* field that lack X-ray counterparts, listed in Table 4.

The two subsamples based on candidate X-ray sources are numbered sequentially 1–386 by increasing R.A. in Table 3. The infrared selected subsample is numbered sequentially 387–441 in Table 4.

The spatial distribution of IRAS 09002-4732 members is placed into a wider context in Figure 1 that includes both the IRAS 09002-4732 region and the MYStIX target H II region RCW 38 to the west. MIREs disk-bearing candidates from Povich et al. (2013) are shown as cyan (Class II/III) and red (protostars) symbols. Recall that both RCW 38 and IRAS 09002-4732 have bright infrared nebosity from H II region emission lines and heated dust; this considerably reduces the sensitivity of the infrared surveys, causing the MIREs infrared-excess catalog to be very incomplete.

3.3. Star Formation along the Molecular Filament

Examination of Figure 1 immediately reveals that the spatial distribution of the MIREs stars, selected to have infrared spectral energy distributions consistent with low-mass protostars, is strongly elongated along a northwest–southeast axis (approximately along P.A. 110° east of north). The northwest direction points toward the large RCW 38 cloud, and the southeast direction is along a thin dusty filament with a small cloud condensation a few arcminutes outside the *Chandra* field of view. This strongly suggests that current star formation is concentrated along a filament several parsecs long. On a smaller scale of 0.5–1 parsec around the IRAS 09002-4732 cluster core, the VLT-ISAAC *JHK* image presented by Apai et al. (2005) shows dense obscuring cloud structure along the same northwest–southeast axis.

A similar spatial trend is present in the ages of X-ray selected members, as inferred from the presence or absence of an infrared-emitting inner circumstellar disk. Recall that X-ray selection of PMS stars is largely independent of disks, as it arises from magnetic reconnection flares. Figure 4 shows the 386 ACIS sources with colors representing the presence of disk emission in the spectral energy distributions obtained from 2MASS *JHK* and *Spitzer* IRAC 3.6– $8.0 \mu\text{m}$ photometry. A disk is inferred to be present when the infrared power-law slope exceeds -1.9 (Richert et al. 2018). The disk-bearing stars show a clear tendency to lie along the northwest–southeast axis, while the disk-free or undetermined cases (due to inadequate infrared photometry in the nebular region) exhibit a more spherical distribution.

The MIREs stars in the filament are not strongly concentrated into groups or clusters, but rather appear to be reflect a condition of distributed star formation. This differs from other situations in the massive MYStIX star-forming regions where embedded small clusters are common in the vicinity of a revealed rich cluster (Kuhn et al. 2014; Getman et al. 2018a). There are other cases where infrared-excess stars are mostly found in groups, such as the large infrared dark cloud G53.2 at a distance similar to IRAS 09002-4732 (Kim et al. 2015).

3.4. Identifying Clusters

As mentioned in Section 3.1, we apply a statistical procedure developed by Kuhn et al. (2014) for identifying stellar clusters in two-dimensional spatial point distributions. The method is based on maximum likelihood estimation of a mixture model where, instead of the usual Gaussian shape, we assume each cluster can be represented by an isothermal ellipsoid with a central surface density σ_0 , core radius r_c , ellipticity ϵ , and orientation θ . The ellipticity is defined to be $(a - b)/a$, where a and b are the major and minor axes, respectively. The optimal number of clusters k of the model is obtained by maximizing the Akaike Information Criterion, a widely used penalized likelihood measure for selecting parsimonious models. Ellipsoidal components can be disjoint, overlapping, or with a small component encompassed within a larger one.

The best-fit model for the 441 spatial distribution of X-ray and infrared selected members of the IRAS 09002-4732 region (Section 3.2) is shown in Figure 5. The majority stars are members of a compact cluster centered at $(09^{\text{h}}01^{\text{m}}54^{\text{s}}.2, -47^{\circ}43'48'')$. This is $23''$ north of the dominant O7 star and the radio continuum peak, lying between dense filaments S2 and S3 that obscure the cluster center; see Apai et al. (2005), and our Appendix A. This cluster has major and minor axis core radii 0.08×0.14 pc ($\epsilon = 0.43$) with $\theta = 143^{\circ}$ east of north.

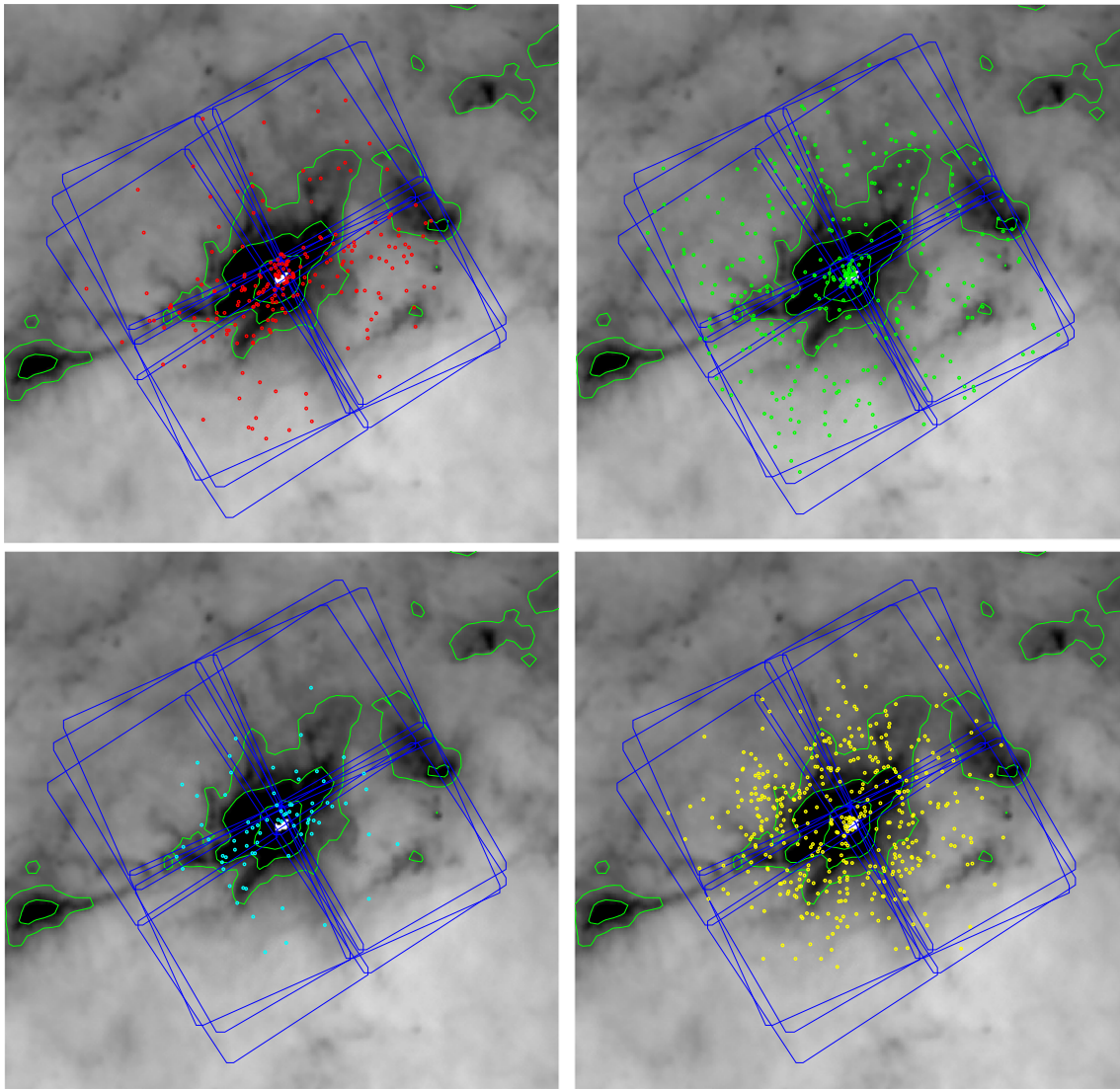


Figure 3. Spatial distribution of four subsamples of candidate X-ray sources superposed on a *Herschel* SPIRE 250 μm map of the IRAS 09002-4732 region. The green contours represent infrared surface brightness levels of 500, 1000, and 3000 MJy sr^{-1} ; these show the shape of the dusty cloud structures. The candidate X-ray sources are divided into subsamples and colors following Figure 2. See the text for details.

The remaining stars are members of a more elongated, lower-density cluster centered at $(09^{\text{h}}01^{\text{m}}53^{\text{s}}.7, -47^{\circ}44'16'')$. This cluster has major and minor axis core radii 1.45×0.23 pc ($\epsilon = 0.84$) with $\theta = 111^{\circ}$.

Judging from the results of the SFiNCs Monte Carlo simulations (Getman et al. 2018b, their Figure 5), the formal fractional errors on the inferred cluster core radii and ellipticities in IRAS 09002-4732 should not exceed 20%. The elongated cluster component clearly delineates the findings in Section 3.3 that star formation is concentrated in a northwest–southeast molecular filament. There is no statistically significant substructure in either grouping, and there is no significant uniformly distributed unclustered stellar population from an earlier generation of star formation.

The central surface density of the compact cluster is ~ 20 times higher than the elongated cluster, but its spatial extent is smaller. It is thus difficult to decide on their relative populations, or to assign specific stars to one or the other component. We roughly estimate that 80% of the stars belong to the compact cluster and 20% belong to the protostellar population.

4. Properties of Clusters and Individual Stars

4.1. Distance

Historical estimates of the distances to Galactic Plane star-forming regions typically vary considerably. For IRAS 09002-4732, Lenzen (1991) adopts 1.8 kpc, Ghosh et al. (2000) have a best fit of 1.4 kpc to the embedded O7 star, and Apai et al. (2005) assume 1.3 kpc. Our MYStIX project assumed 1.7 kpc for RCW 38 (Feigelson et al. 2013), following the review by Wolk et al. (2008). Today, however, for a small fraction of member stars that are sufficiently bright in the optical band, the DR2 catalog of ESA’s *Gaia* satellite provides direct measurements of parallax distance (Gaia Collaboration et al. 2016, 2018).

Gaia parallaxes to PMS members of IRAS 09002-4732 and its neighboring RCW 38 cluster are shown Figure 6, restricted to stars with respective parallax errors less than ~ 0.1 mas and ~ 0.13 mas for the two regions. The sample includes 18 members of RCW 38 from the MYStIX Probable Complex Members (Broos et al. 2013) and 20 members of IRAS 09002-

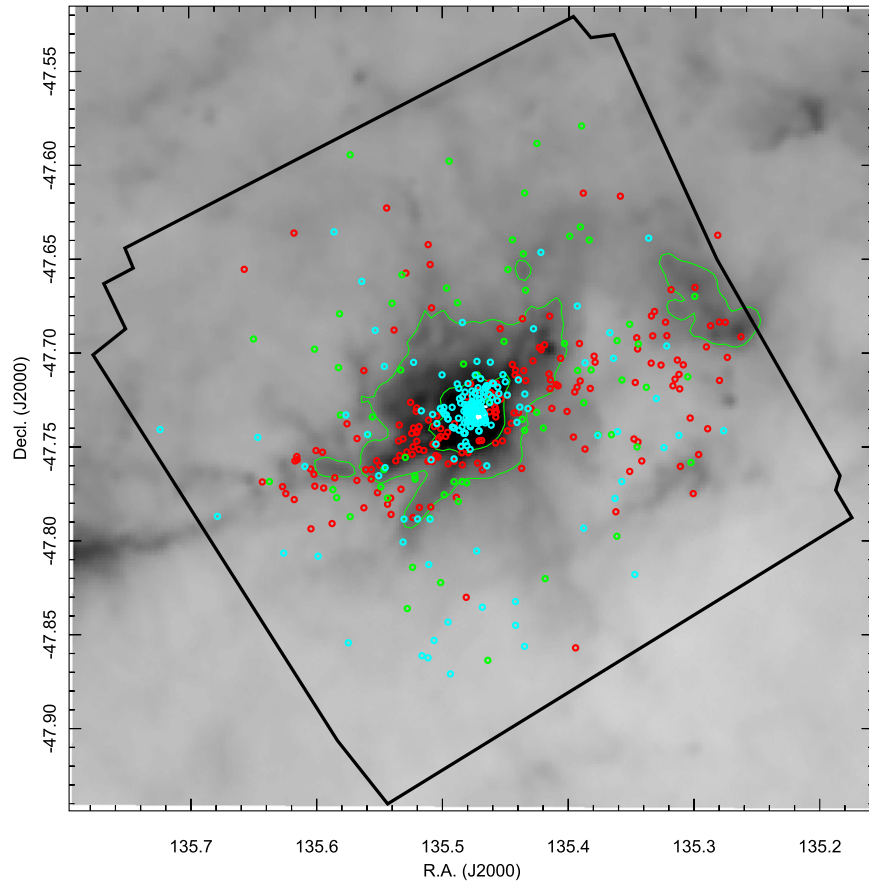


Figure 4. Spatial distribution of 386 X-ray selected PMS members coded by disk infrared emission as an indicator of stellar age: disk present (red symbols), disk absent (green), and undetermined (cyan).

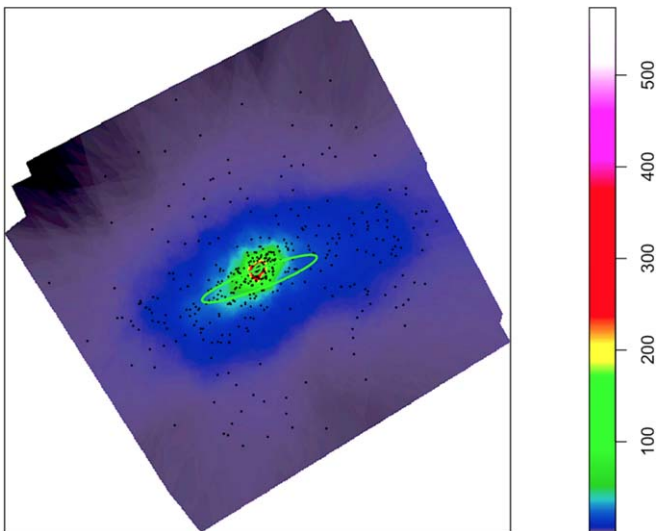


Figure 5. Maximum likelihood mixture model fit decomposing the spatial distribution of 441 PMS members into two components. The color map shows an adaptively smoothed image with a color bar in units of observed stars pc^{-2} . Black dots indicate the individual stars, and the green ellipses show the core radii of the two ellipsoidal components.

4732 identified here. The parallax distribution appears to have outliers, perhaps due to contamination by nebulosity. A concentration is seen around $0.55\text{--}0.60$ mas, corresponding to $1.7\text{--}1.8$ kpc. For consistency with our MYStIX study, we adopt a distance of 1.7 kpc for this study.

4.2. Extinction

The IRAS 09002-4732 cluster is known to be highly extinguished: the stars and emission nebulosity are obscured by dense dusty filaments and globules with characteristic obscuration around $A_V \simeq 20$ mag, individual PMS stars exhibit extinction ranging from $A_V \simeq 3$ to 30 mag, and a $9.7\ \mu\text{m}$ absorption feature in the ultracompact H II region corresponds to $A_V \simeq 20$ mag (Apai et al. 2005). Lenzen (1991) infer a higher absorption of $A_V > 45$ mag, and possibly $A_V > 70$ mag, from the spectral energy distribution of the dominant O7 star.

X-ray emission in the *Chandra* $0.5\text{--}8$ keV band is sensitive to line-of-sight absorption by interstellar material. Here, the effect is mostly due to bound-free photoionization of gas-phase metal atoms, not to scattering and absorption effects of solid grains as in the OIR bands (Wilms et al. 2000). Getman et al. (2010) have calculated a conversion between this absorption of softer X-rays and the observed median energy of a PMS star, assuming a typical PMS flare spectrum and the spectral response of the *Chandra* mirror and ACIS detector, giving estimates of hydrogen column densities $\log N_H$ for individual X-ray sources (Table 3). Most stars lie in the range $21.8 < \log N_H < 23.3\ \text{cm}^{-2}$ with median value of $22.4\ \text{cm}^{-2}$. Adopting a gas-to-dust ratio $N_H/A_V = 2 \times 10^{21}\ \text{cm}^{-2}\ \text{mag}^{-1}$ (Zhu et al. 2017), this corresponds to a range of $3 \lesssim A_V \lesssim 100$ mag with median value $A_V \simeq 13$ mag.

The absorption to the X-ray selected IRAS 09002-4732 members exhibits a strong spatial gradient shown in Figure 7. The right panel shows an adaptively smoothed map of the mean

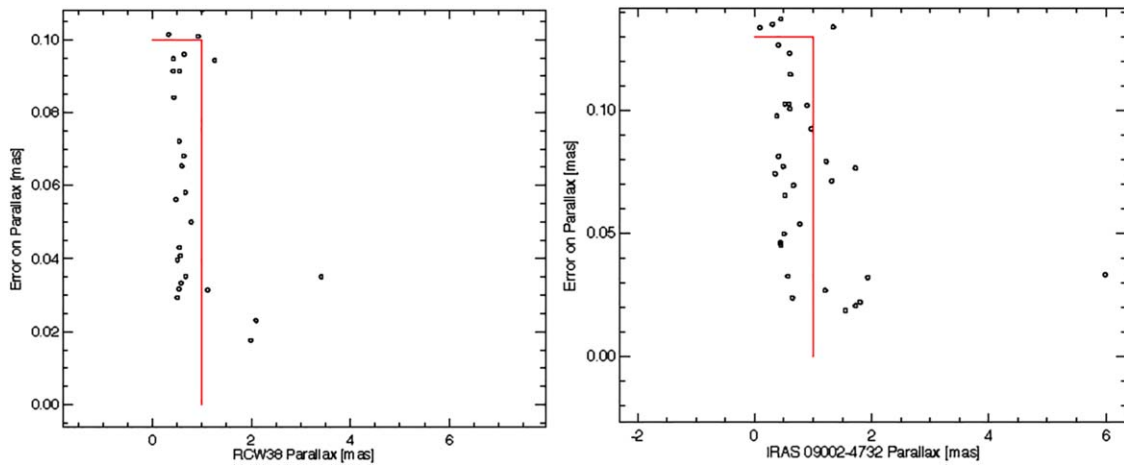


Figure 6. Parallax measurements of PMS members of RCW 38 (left) and IRAS 09002-4732 (right) from the *Gaia* DR2 catalog. To guide the eye, the vertical red lines show the parallax value of 1 mas and the horizontal red lines show errors of 0.10 mas (left) and 0.13 mas (right), respectively. These values are not corrected for any systematic shift.

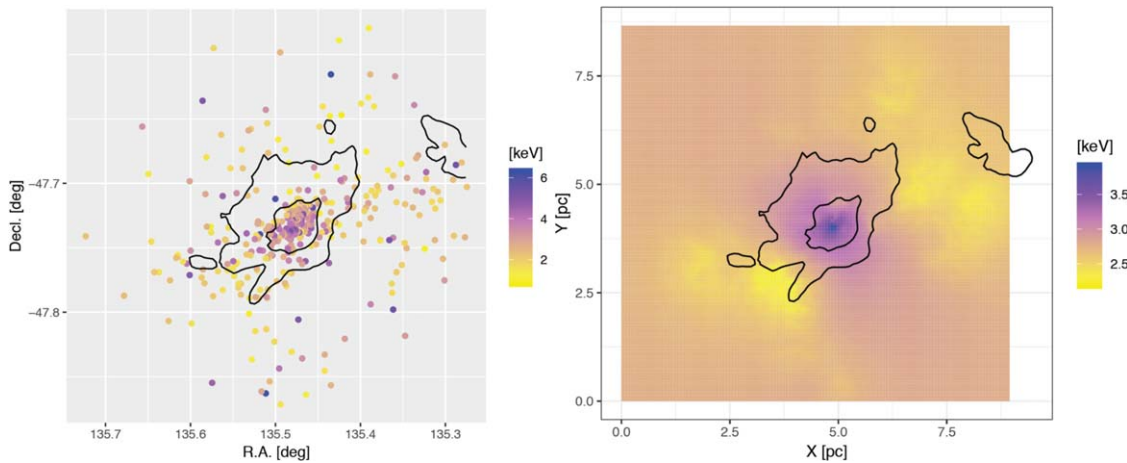


Figure 7. Spatial distribution of interstellar extinction to X-ray selected members of IRAS 09002-4732, based on observed median energy of photons from each source. The left panel shows individual source median energies with celestial coordinates, while the right panel shows an adaptively smoothed mean value with parsec coordinates, assuming a distance of 1.7 kpc. The contours are based on surface brightness of the *Herschel* 250 μm map.

median energy values.⁷ Stars on the periphery of the *Chandra* field, with projected distances exceeding ~ 1 pc, show typical absorptions around $A_V \simeq 10\text{--}20$ mag, considerably lower than stars concentrated in the cluster center that reach $A_V \simeq 50$ mag.

4.3. Age

We provide age estimates for individual stars using two different chronometers for subsamples of the IRAS 09002-4732 stellar population:

1. Getman et al. (2014) present the Age_{JX} estimator for individual PMS stars, based on absorption-corrected X-ray luminosity, dereddened J magnitudes, distance, and standard PMS evolutionary tracks (Siess et al. 2000). As this requires both high-quality X-ray and near-infrared photometry, it can be calculated for only 22 stars located around the central cluster. For this subsample, the median age is $\text{Age}_{JX} = 0.8$ Myr.

2. Forty-five stars with low absorption that are dispersed around the central cluster have optical band photometry from the VPHAS+ survey. Their r_0 versus $r_0 - i_0$ color-magnitude diagram is shown in Figure 8, along with the Siess et al. (2000) tracks and their spatial distribution. Here, we see a range of ages from <0.1 Myr to 3 Myr, with a median around 0.7 Myr. Some of these are widely distributed and others probably lie in the molecular filament; stars in the cluster core are underrepresented due to difficulties of high obscuration and bright nebulosity.

We thus estimate an average age of 0.8 Myr for the central cluster of IRAS 09002-4732, with a range of <0.1 to ~ 3 Myr for individual stars. The protostars distributed along the molecular filament are undoubtedly younger, and it is reasonable to assign them an age around 0.1 Myr.

Many young clusters exhibit an age gradient in Age_{JX} , in the sense that the cluster cores appear younger (that is, they formed stars later) than the peripheries of the clusters (Getman et al. 2018a). There is some evidence for this from Figure 4, where the older disk-free stars (green symbols) are more widely distributed than the concentrated cluster. However, due to

⁷ This map is calculated with the function *adaptive.density* in package *spatstat* within the public domain R statistical software environment (Baddeley et al. 2015).

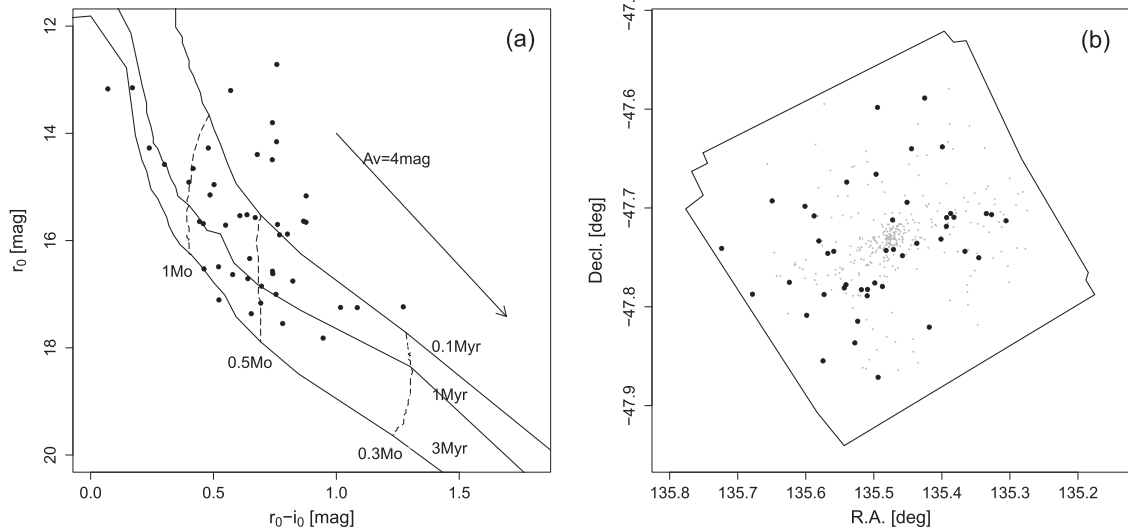


Figure 8. Optical color–magnitude diagram (a) and spatial distribution (b) for 45 stars around the IRAS 09002-4732 cluster, used for estimation of stellar ages.

nebulousity and obscuration, insufficient infrared photometry is available in the central region to check whether the disk fraction is higher in the cluster core.

4.4. Total Stellar Population

The XLFs of young ($t \leq 5$ Myr) PMS populations show no apparent variation between different star-forming regions. They exhibit shapes consistent with the ONC, where the full population is nearly entirely detected with very high sensitivity from the 838 ks observation of the *Chandra* Orion Ultradeep Project. The truncated XLF of a distant region observed with short *Chandra* exposures can therefore be calibrated to the ONC’s complete XLF, in order to obtain the total stellar population (in units of ONC’s population). This procedure is described and applied to 16 major star-forming regions by Kuhn et al. (2015b).

The results for IRAS 09002–4732 are shown in Figure 9. The solid histogram shows the distribution of total-band (0.5–8 keV), absorption-corrected X-ray luminosities for 839 lightly-obscured ($\log N_{\text{H}} < 22.0 \text{ cm}^{-2}$) stars with spectral types cooler than B4 from the *Chandra* Orion Ultradeep Project (Getman et al. 2005). These are the $\log L_{t,c}$ values for the “lightly obscured cool stars” in Table 1 of Feigelson et al. (2005). The dashed histogram shows the distribution of L_X values for the 386 IRAS 09002-4732 *Chandra* stars. The sample becomes incomplete below $\log L_X \simeq 31.0 \text{ erg s}^{-1}$, but the region clearly has more X-ray stars with $\log L_X \sim 31\text{--}32 \text{ erg s}^{-1}$ than does the ONC.

A maximum likelihood fit to a power-law distribution for $\log L_X \geq 31.0 \text{ erg s}^{-1}$ with slope 0.9 gives a normalization factor of 2.3; that is, the IRAS 09002-4732 region shown in Figure 4 contains more than twice the unobscured population of the ONC. If the ONC has an estimated population of 2600 stars, down to the stellar limit of $0.08 M_{\odot}$ (Kuhn et al. 2015b), then the IRAS 09002-4732 region has ~ 6000 stars. If we adopt that 80% of the stars belong to the compact cluster and 20% belong to the protostellar population, as discussed in Section 3.4, then the total population of the main cluster is ~ 5000 stars and the total population of the younger component in the molecular filament is ~ 1000 stars within the *Chandra* field of view.

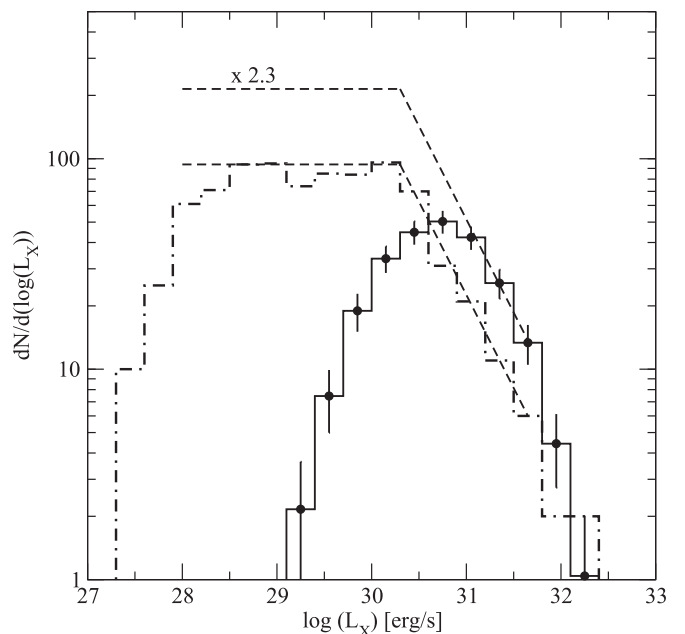


Figure 9. Calibration of the IRAS 09002-4732 X-ray luminosity function (solid histogram) to the XLF of the Orion Nebula Cluster (dotted–dashed histogram). The two dashed lines show the offset in population between the two clusters.

5. Discussion

5.1. Comparison with Other Rich Young Clusters

The central IRAS 09002-4732 cluster resembles other rich MYStIX clusters modeled by Kuhn et al. (2014, 2015b). It shows morphology and population similar to RCW 38, Trumpler 14 in the Carina complex, NGC 6616 in the Eagle Nebula, and the ONC in the Orion complex. All of these clusters have several thousand total stars and exhibit a core-halo structure where the central isothermal ellipsoidal component has core radius $r_c \simeq 0.1 \text{ pc}$. IRAS 09002-4732 differs from the others in three respects:

1. The ellipticities of both the core and halo components in IRAS 09002–4732 are higher than in the other clusters,

Table 5
Comparison of IRAS 09002-4732 and Orion Nebula Cluster Properties

Cluster	$\log r_4$ pc	$\log n_4$ stars	$\log \Sigma_0$ stars pc ⁻²	$\log \rho_0$ stars pc ⁻³	ϵ ...	ME (keV)	log Age (yr)
IRAS 09002-4732							
Cluster	-0.37	3.57	4.55	5.22	0.43	2.5–5	5.85
Protostars	0.36	2.96	2.49	2.43	0.84	...	5.0:
Orion Nebula							
Cluster core	-0.71	2.17	3.85	4.86	0.30	1.6	6.04
Cluster halo	-0.06	3.21	3.58	3.94	0.49	1.6	6.18
Protostars	-0.44	1.94	3.07	3.81	0.84	1.4	5.0:

where core ellipticities are $\epsilon \lesssim 0.3$ (rather than 0.43) and halo ellipticities are $\epsilon \lesssim 0.5$ (rather than 0.84).

- IRAS 09002-4732 is more heavily absorbed than the Carina, Eagle, and Orion clusters, with A_V reaching ~ 50 mag in the cluster core, compared to $A_V < 5$ mag for the other cases. Only RCW 38 shows similarly high absorption.
- Except for RCW 38, IRAS 09002-4732 is younger than the comparison clusters, with $\text{Age}_{JX} \sim 0.8$ Myr versus a more typical $\text{Age}_{JX} \sim 2$ Myr. Appendix B presents new evidence that RCW 38 has a very young age, similar to that of IRAS 09002-4732.

IRAS 09002-4732 and RCW 38 thus resemble some of the richest young stellar clusters in the nearby Galactic Plane, but seen at an earlier stage of evolution, with less time for dynamical equilibration (hence their higher eccentricity) and less time for destruction of the molecular environment (hence their higher absorption). This latter effect is also reflected in the size of the ionized H II region: Orion and Eagle have giant H II regions > 1 pc in extent, while IRAS 09002-4732 and RCW 38 have UltraCompact H II regions only $\simeq 0.1$ pc in extent (Apai et al. 2005).⁸

Table 5 provides a more quantitative comparison of the IRAS 09002-4732 stellar population to the ONC region. As outlined in Section 1, the Orion region has motivated much of the astrophysical discussions of cluster formation (Krumholz et al. 2019; Vázquez-Semadeni et al. 2019). Combining the ellipsoidal structural parameters obtained in Section 3.4 and the estimates of total population in Section 4.4, cluster physical parameters can be derived following Kuhn et al. (2015b, 2015a). The quantities compared are: a characteristic radius $r_4 = 4r_c$ in units of pc, roughly corresponding to the projected half-mass cluster radius; the total stellar population within this radius, n_4 ; the stellar surface density Σ_0 within this radius in stars pc⁻²; and the central stellar density ρ_0 within this radius in stars pc⁻³. In Table 5, the Orion Nebula “Cluster core” corresponds to the small and dense Trapezium component, the “Cluster halo” corresponds to the main portion of the ONC, and the rows labeled “Protostars” correspond to the north–south molecular filament pointing toward the OMC-2/3 star-forming region. A fourth elliptical component corresponding to the Becklin–Neugebauer/Kleinman–Low protostellar cluster in the OMC-1 cloud behind the ONC is omitted here.

As with our preview examination, Table 5 shows that the IRAS 09002-4732 cluster is richer, more embedded, and younger than

the ONC. Its core radius is intermediate between the ONC Trapezium and ONC halo components. The inferred central star density is thus extremely high, $\rho_0 \simeq 1.5 \times 10^5$ stars pc⁻³. This is similar to the central density inferred for RCW 38, $\rho_c \simeq 2 \times 10^5$ stars pc⁻³ (Kuhn et al. 2015a). If the ONC Trapezium experienced close stellar encounters and dynamical ejections, as suggested by its anomalous mass function and repeated episodes of core star formation (Pflamm-Altenburg & Kroupa 2006; Wang et al. 2019), then similar stellar interactions may be present in IRAS 09002-4732 today.

Both the IRAS 09002-4732 and ONC rich clusters have substantial ellipticity, with the former around $\epsilon \simeq 0.6 = 0.7$ and the latter around $\epsilon \simeq 0.3\text{--}0.5$. However, their associated protostellar populations have even higher ellipticities ($\epsilon \simeq 0.8\text{--}0.9$); these spatial distributions can be considered to be “filamentary” (Getman et al. 2018b). Furthermore, in both cases, the protostars are embedded in filamentary molecular cloud structures. This contrasts with older rich clusters, such as NGC 6231 (Kuhn et al. 2017) and NGC 2244 in the Rosette Nebula (Kuhn et al. 2015a), that are much larger and nearly spherical. *Gaia* proper motions show that these (and other) older young clusters are dynamically expanding from an earlier compact state (Kuhn et al. 2019).

The physical properties of the central cluster of IRAS 09002-4732 (Section 4) can also be compared to the full sample of MYStIX (sub)clusters by placing it on the bivariate scatter plots shown in Figure 1 of Kuhn et al. (2015b). For some properties, the central cluster follows trends of young age, high absorption, small radius, and high central star density. However, it has an unusual combination of other properties. Trumpler 14 in the Carina Nebula and NGC 6611 in the Eagle Nebula are nearly as rich as IRAS 09002-4732, but they are older and less absorbed, with core radii several times larger and consequently much lower central star densities. In the case of NGC 6611, analysis of *Gaia* proper motions (Kuhn et al. 2019) shows there to be clear evidence of kinematic expansion from a more compact morphology. The core of RCW 38 is the closest match to the IRAS 09002-4732 central cluster, with similarly high population, young age (Appendix B), small radius, and high central star density. We also note that M 17 is very rich and centrally condensed—but its morphology is “clumpy,” without a single component that dominates the population.

We can also seek analogs to IRAS 09002-4732 based on the early evolutionary stage of its H II region. The ultracompact H II region requires that its most massive member is extremely young and/or just recently encountered the molecular environment. Most heavily obscured young clusters have relatively large H II regions, such as the less rich W 40 (Rodney & Reipurth 2008) and the Flame Nebula (Bik et al. 2003), with

⁸ The small evacuated bubble around the dominant star of RCW 38 is shown by DeRose et al. (2009). Trumpler 14 does not produce an H II region, because it is born in a complex where supernova remnants have previously dissipated most of the molecular material (Townsend et al. 2011b, 2011a).

~ 1 pc extent of the ionized radio continuum region. W3-Main, however, is a rich older cluster with a remarkable assemblage of HII regions ranging from hypercompact ($\lesssim 0.003$ pc) to giant ($\simeq 0.5$ pc) in size (Tieftrunk et al. 1997; Feigelson & Townsley 2008; Bik et al. 2014). Collectively, the evidence suggests that massive star formation can occur over a long timescale, but is sometimes delayed until after most lower-mass stars have formed and assembled into a cluster.

In summary, seven very rich young stellar clusters are present in the nearby Galactic Plane: the ONC, Trumpler 14, NGC 6611, M17, W3 Main, RCW 38, and IRAS 09002-4732. Some have very dense cores, with $\gtrsim 10,000$ stars pc^{-3} , while others are more extended and have likely expanded from a more compact state. IRAS 09002-4732 and RCW 38 represent the earliest stage of evolution, with the highest absorption highest central star density, and youngest stars.

5.2. Implications for Star Cluster Formation

First seen in large-scale CO maps of the Orion complex clouds (Bally et al. 1987; Uchida et al. 1991), filamentary molecular structures are now found on many scales throughout the interstellar medium. The Snake Nebula is an isolated sinuous cloud $\simeq 30$ pc long, with a hierarchy of dense cores on scales 0.1–0.01 pc (Wang et al. 2014). Regions in Aquila Rift are composed of a networks of filaments (Moriguchi et al. 2001; Kusune et al. 2016). The emission line nebula of IRAS 09002-4732 is partly obscured by dark filaments with characteristic lengths around 0.5 pc and widths around 0.05 pc, with scattered small dark globules within (Apai et al. 2005); for a visualization, see the lower right panel of Figure 10. Typically, some filament concentrations are undergoing gravitational collapse with protostars within, while other concentrations are currently stable.

Hydrodynamical models of star formation in realistically turbulent molecular cloud cores show that filaments form quickly, undergoing fragmentation into cores that form small groups of stars (Bate et al. 2003; Federrath 2015; Vázquez-Semadeni et al. 2017, 2019). These groups are dragged into the center of the cloud gravitational potential well as the gaseous filaments infall and merge. In early calculations lasting $\lesssim 1$ Myr, the stars of different ages are efficiently mixed into a homogeneous, quasi-spherical cluster (Bate et al.). However, our empirical research shows that rich clusters show a strong spatial age gradient on timescales of ~ 0.5 –5 Myr, requiring that star formation continue in the cluster cores after cluster formation (Getman et al. 2018a). Some later calculations can explain this effect through a hierarchical filament merging process, combined with stellar feedback, continuing over millions of years (Vazquez-Semadeni et al. 2019). Other models, such as continuous star formation in a cluster fed by a “conveyor belt” of infalling gas (Krumholz & McKee 2019), do not clearly account for the observed stellar age gradients.

Discussion continues with regard to the relative importance of turbulence and thermal pressure, magnetic dynamical effects, low-mass and high-mass stellar feedback onto the collapsing gas, binary star systems, and N -body interactions in the denser cluster cores (Krumholz et al. 2019). Turbulence may play a more limited role than originally thought, but the basic scenario of slow cluster formation via merging filaments seems well-established from an astrophysical perspective, in contrast to older models involving rapid monolithic cluster formation (Elmegreen 2000) or a global exponential burst of star formation (Palla & Stahler 2000).

However, there is little *direct* empirical evidence that demonstrates that *rich* clusters (containing thousands of stars) form with molecular filaments. The ONC is an example of not-infrequent *indirect* associations of an older rich clusters with an origin in filaments. The link is indirect because the molecular material giving rise to the ONC has been destroyed by the giant H II region. First, many sparse groups of protostars are forming today in the contemporary Orion molecular filament (Megeath et al. 2012), although we do not know whether they will consolidate into a rich cluster. Second, the ONC has an elliptical morphology elongated along the filament axis. Third, stars projected against the OMC-1 filament show radial velocities similar to that of the OMC-1 gas; this star-cloud velocity agreement is evident despite a strong velocity gradient along the filament (Getman et al. 2019).

IRAS 09002-4732 is a rare case where a nascent rich star cluster, possessing a massive O star and thousands of PMS stars, is embedded in a molecular filament. Apai et al. (2005) analyze the three-dimensional environment and conclude that the cluster lies between dense cores; that is, the cluster is truly embedded and not just obscured behind a screen of cloud material. The H II region of the dominant O7 star is in the ultracompact stage, suggesting that the star formed very recently, perhaps in the past 10^4 yr. While the average age of the cluster stars is ≤ 0.8 Myr (Section 4.3), an age gradient is quite possibly present (Getman et al. 2018a) and the central core may be actively forming stars today. The surrounding natal molecular environment is in the process of being heated and ejected, and the stellar density in the cluster core is so high (Section 5.1) that high-velocity N -body interactions (or even stellar collisions) should be occurring. This recent and rapidly evolving activity takes place within a molecular filament several parsecs in extent that exhibits mild, distributed star formation outside of the central cluster.

5.3. Initial Mass Function of IRAS 09002-4732

Finally, we note that the IRAS 09002-4732 cluster may have an anomalous IMF, in the sense that it is deficient in massive stars. If it truly has a stellar population 2–3 times that of the ONC, which itself may lack a full complement of O stars, then it is expected to have more massive stars. A standard IMF with a Salpeter power-law tail is expected to have $\simeq 20$ stars above $M = 10 M_{\odot}$ and 2–3 stars above $M = 30 M_{\odot}$, for a population around 5000–8000 stars (Section 4.4) above the stellar limit (Kroupa 2001). We would thus expect to see a collection of small H II regions in the cluster core rather than just one around Source D.

If this deficiency of massive stars is real, two explanations are plausible. First, the stars may have formed but are now ejected by dynamical interactions with other massive stars. Rapid dynamical decay has been calculated to be responsible for the deficit of massive stars in the ONC core (Pflamm-Altenburg & Kroupa 2006; Allen et al. 2017; Wang et al. 2019), which we estimate is less dense than the core of IRAS 09002-4732 (Table 5). This hypothesis can be empirically tested by a search for stars recently ejected from the cluster core in the *Gaia* proper motion database. Second, it is possible that massive stars other than Source D have not yet formed. There is evidence for delayed O star formation in the ONC (O’Dell et al. 2009), W3 Main (Tieftrunk et al. 1997; Feigelson & Townsley 2008; Bik et al. 2014), and M17 SW (Povich et al. 2016). This picture is consistent with the global hierarchical gravitational collapse postulated by Vázquez-Semadeni et al. (2019), who explain late

massive star formation in the central potential well and later destruction of filamentary gas feeding by OB stellar feedback.

6. Conclusions

We obtain a new census of PMS stars for the IRAS 09002-4732 star-forming region from a deep observation with the *Chandra X-ray Observatory*. In concert with existing OIR catalogs, 386 probable members with subarcsecond positions are identified (Table 3), both within the central cluster and in the surrounding cloud. These are supplemented by 55 non-X-ray infrared-excess stars (Table 4). The sample selection, following procedures from our MYStIX and SFiNCs surveys, has low contamination by Galactic field stars or quasars. Measures of magnetic activity ($\log L_x$ obtained from X-ray photometry), absorption ($\log N_H$ and A_V from X-ray median energy), age (Age_{IX} from X-ray and near-infrared photometry, and optical ages from an $r-i$ color-magnitude diagram), and disk presence (from near- and mid-infrared photometry) are calculated for the 441 individual stars.

From this information, collective properties of the cluster and star-forming environment are inferred:

1. The stars have a distinctive bipartite spatial structure. Most members reside in a compact, elliptical rich cluster with core radius 0.1 pc centered 0.15 pc north of Source D, the O7 star that dominates the light from the cluster. A minority reside in a loose, highly elongated (eccentricity $\sim 90\%$) distribution oriented northwest-southeast around the cluster. This coincides with a molecular filament several parsecs long that connects to the nearby, larger molecular cloud hosting the rich RCW 38 young star cluster (Sections 3.3 and 3.4).
2. The distance to the member stellar population is approximately 1.7 kpc, evaluated from *Gaia* parallax measurements. This is consistent with most previous distance estimates (Section 4.1).
3. The stellar population is heavily absorbed, with median absorption $A_V \simeq 13$ mag. The extinction increases sharply to $A_V \simeq 50$ mag at the cluster center (Section 4.2).
4. The average age of the member population, both from X-ray/infrared photometry (Age_{IX}) and from an $r-i$ color-magnitude diagram, is ~ 0.8 Myr, calibrated to the evolutionary tracks of Siess et al. (2000). However, the filament-associated elongated population is younger, as it is identified by several dozen protostars, and a spatial gradient in age within the main cluster may also be present. Source D may also be very young, as its H II region is very small (ultracompact), with an extent of only 0.1 pc (Sections 4.3 and 5.1).
5. The stellar population is remarkably large. The total population deduced from the XLF is twice that of the ONC, or roughly 5000 stars (Section 4.4).
6. The cluster core is incredibly dense, with $\sim 1.5 \times 10^5$ stars pc^{-3} . This is a regime where strong N -body interactions should be common, causing destruction of binaries, high-velocity ejection of runaway members, and possibly stellar collisions (Sections 5.1 and 5.3).
7. In morphology and population, the IRAS 09002-4732 cluster resembles some of the richest young clusters in the solar neighborhood: ONC in the Orion Nebula, Trumpler 14 in Carina, NGC 6611 in Eagle, M17 in Omega, W3 Main in W 3, and the nearby RCW 38. However, IRAS 09002-4732 and RCW 38 are distinctively younger and more heavily

absorbed (with less time for stellar feedback to disperse the gas), with higher ellipticity (with less time for dynamical equilibration) and smaller H II regions (Section 5.1).

8. The IMF of the cluster appears to be deficient in massive stars. Either OB stars similar to Source D have not yet formed, or they have been dynamically ejected by N -body interactions in the dense core (Section 5.3).

We conclude that IRAS 09002-4732 is a rare case where a rich (thousands of stars) cluster is forming today in a molecular filament. More commonly, either the cluster is embedded but sparse (dozens of stars) or the rich cluster has already destroyed its natal molecular environment. The stellar spatial distribution, individual properties (ages, extinction), and collective properties (population, IMF, cluster structure) directly support contemporary numerical calculations of cluster formation in clouds that involve the hierarchical formation and merging of groups in molecular filaments, such as those described by Vázquez-Semadeni et al. (2019) and Krumholz et al. (2019).

The IRAS 09002-4732 cluster, particularly the core with radius $1'.5$ centered at $(\alpha, \delta) = (135^\circ.47435, -47^\circ.72820)$, thus warrants future study as an important laboratory for the study of cluster formation in molecular filaments. The most crucial observations needed are high-quality molecular maps obtained with the ASTE and ALMA telescopes that might show gravitational infall of gas, either along or perpendicular to the filament axis. In the immediate proximity of the cluster, combinations of gas infall to fuel star formation and gas outflow in response to stellar feedback may be occurring. The complicated gas kinematics that may be present could benefit from study with advanced instruments like the optical band MUSE integral field spectrograph on the Very Large Telescope, or the NIRSpect spectro-imager on board the *James Webb Space Telescope*. For the stellar population, the *Gaia* catalog can be searched for high-velocity stars ejected from the core, and infrared multi-object spectroscopy of cluster members can elucidate its dynamical state. Deeper *Chandra* observations would identify a larger fraction of the PMS stellar population both in the cluster and the surrounding filamentary cloud. We also recommend further study of the gas and stellar content of W3 Main, another rare case of an embedded rich star cluster where the diversity of H II regions points to continuing star formation in the cluster core (Feigelson & Townsley 2008).

The first two authors contributed equally to this study. We benefited from crucial earlier work by Matt Povich (California State Polytechnic University, Pomona), valuable discussion with Daniel Apai (Arizona), and the insightful comments of an anonymous referee. This work was supported by NASA grants GO7-18001X and the Chandra ACIS Team contract SV474018 (G. Garmire and L. Townsley, Principal Investigators), issued by the Chandra X-ray Center, which is operated by the Smithsonian Astrophysical Observatory for and on behalf of NASA under contract NAS8-03060. The Guaranteed Time Observations (GTO) data used here were selected by the ACIS Instrument Principal Investigator, Gordon P. Garmire, of the Huntingdon Institute for X-ray Astronomy, LLC, which is under contract to the Smithsonian Astrophysical Observatory; Contract SV2-82024.

This work has also made use of data from the European Space Agency (ESA) mission *Gaia*, processed by the *Gaia* Data Processing and Analysis Consortium (DPAC). Funding for the DPAC has been provided by national institutions, in particular the institutions participating in the *Gaia* Multilateral Agreement.

This publication makes use of data products from the Two Micron All Sky Survey, which is a joint project of the University of Massachusetts and the Infrared Processing and Analysis Center/California Institute of Technology, funded by the National Aeronautics and Space Administration and the National Science Foundation. This research has made use of NASA’s Astrophysics Data System Bibliographic Services and SAOImage DS9 software developed by Smithsonian Astrophysical Observatory.

Appendix A Core of IRAS 09002-4732

While it has long been established that IRAS 09002-4732 is dominated by an O7 star with high luminosity, $L \simeq 1 \times 10^5 M_{\odot}$ (Lenzen 1991), high-resolution infrared imaging with ESO’s Very Large Telescope demonstrates that the core has a dense concentration of OB stars (Apai et al. 2005) that is surrounded by a cluster of lower-mass PMS stars. Our *Chandra* ACIS images have similar resolution and detect a considerable sample of cluster members. This provides a motivation to compare the *Chandra* and VLT images.

The dominant star in the cluster is located at $09^{\text{h}}01^{\text{m}}54^{\text{s}}45-47^{\circ}44'11''0$ (J2000), with designations IRAS 09002-4732, IRS8 (Lenzen 1991), S13 (Ghosh et al. 2000), Source D (Apai et al. 2005), and 2MASS J090154447-4744112. We will call this “Source D” following Apai et al. (2005), noting that the SIMBAD database does not make all of these associations. The 2MASS star is bright in the $2 \mu\text{m}$ band, with $K = 11.4$, but is heavily reddened, with $J - K > 5.5$ ($A_V > 11$ mag). With flux density $\sim 15,000$ Jy at $100 \mu\text{m}$, it is one of the most luminous infrared sources of the Vela molecular clouds. For comparison, the infrared-brightest protostar in the nearby molecular filament is sequence #386, associated with MCP RCW38 69 = 2MASS J09020115-4744563 = MSX6C G268.4452-00.8442 = [MHL2007] G268.4452-00.8442 1 (Romine et al. 2016). At $10.4 \mu\text{m}$, the dominant cluster star has flux density 38.3 Jy while the brightest protostar has 0.27 Jy (Mottram et al. 2007).

Figure 10 illustrates the complicated relationship between the X-ray and infrared samples in two small portions of the IRAS 09002-4732 cluster: the top panels depict a $20''$ region

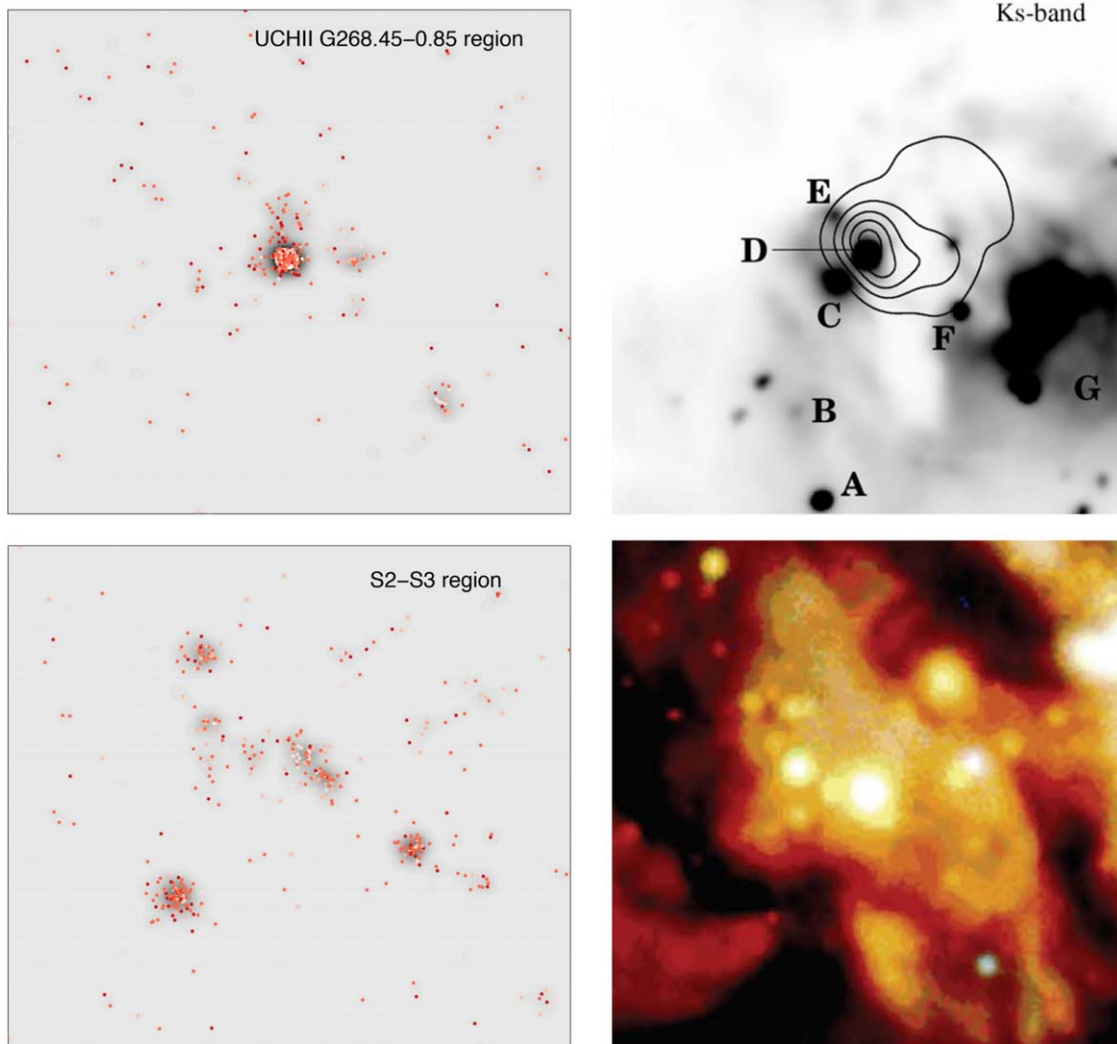


Figure 10. Comparison of X-ray and infrared images for two small regions in the core of IRAS 09002-4732. Each image subtends $20'' \times 20''$ Top: Source D and the ultracompact H II region G268.45-0.85, *Chandra* ACIS and VLT/ISAAC K_s band (Apai et al. 2005). Bottom: A low-obscuration window between dust filaments S2 and S3; *Chandra* ACIS and a VLT/ISAAC *JHK* composite image. The ACIS image shows individual photons, with redness indicating hardness (typical energies 2–7 keV), superposed on a grayscale map smoothed with a $\sigma = 1''$ Gaussian kernel. The upper right panel shows radio continuum contours delineating the ultracompact H II region. The lower right panel shows the S2 and S3 sinuous dusty filaments.

around Source D with its radio ultracompact H II region (top panels), and the bottom panels show a $20''$ region of lower obscuration between the dust filaments S2 and S3 discussed by Apai et al. (2005). Even with a 100 ks exposure, the *Chandra* image is photon-limited; sources with $\simeq 5$ photons are confidently detected, while those with $\sim 2\text{--}4$ photons are possible sources. We also recall that the *Chandra* exposure map shows small-scale variations in exposure times due to satellite dithering motions of the CCD chip gaps.

Source D is not detected in the X-ray band. The nearest sources are Seq #190 (090154.33-474410.3, $\log L_x \simeq 31.9$ erg s $^{-1}$) and #202 (090154.63-474411.1, $\log L_x \simeq 31.2$ erg s $^{-1}$), which respectively lie $1''.5$ NW and $1''.9$ E of the infrared position of Source D (Tables 2–3). These offsets are too large to be attributed to X-ray positional uncertainties ($< 0''.2$) or X-ray/infrared coordinate frame offsets ($< 0''.1$). There is precedence in the Orion region for the X-ray detection of PMS secondary companions but a failure to detect the massive primary. These include the Becklin–Neugebauer Object, where two X-ray stars are detected within a few hundred AU of the luminous high-velocity massive star (Grosso et al. 2005), along with θ^1 Ori B, where the B2.5 primary θ^1 Ori B East would be undetected in IRAS 09002-4732 ($\log L_x = 30.1$ erg s $^{-1}$ with soft X-ray spectrum that can not penetrate high extinction) but the flaring hard X-ray emission produced by binary low-mass companions θ^1 Ori B West would be detected ($\log L_x = 31.5$ erg s $^{-1}$; Stelzer et al. 2005).

Both the infrared and X-ray images show several stars within $\simeq 10''$ of Source D, but the correspondence is not simple. Infrared stars F and G appear as very faint X-ray sources, along with an anonymous star $3''$ west of Source D. The more prominent infrared stars A, B, C, and E are not seen in X-rays. The *Chandra* image shows barely resolved stars $1''\text{--}2''$ east and north of Source D that are not evident in the available infrared images.

The S2–S3 region shown in Figure 10 (bottom panels) also shows both similarities and differences in the two bands. As with Source D above, lower mass members of the region are seen in X-rays while the most luminous infrared member is not detected. The X-ray image shows ~ 9 faint X-ray sources in a chain extending $\sim 15''$ from northeast to southwest. Most of these have discernible counterparts in the VLT infrared image. The brightest X-ray source to the southeast lies embedded in or behind a dark dust lane and is thus missing an infrared counterpart. This source is sequence #227 (090155.50-474355.7) with 46 net counts, absorption-corrected $\log L_x \simeq 31.6$ erg s $^{-1}$, and median energy absorption $ME \simeq 3.9$ keV corresponding to $\log N_H \simeq 9 \times 10^{22}$ cm $^{-2}$ and $A_V \simeq 45$ mag. This star lies near the top of the XLF (Figure 9).

Appendix B Age of RCW 38

Getman et al. (2014) reported that RCW 38, W 40, and the Flame Nebula are the youngest MYStIX star-forming regions, with average ages of $\text{Age}_{JX} \leq 1$ Myr (see their Figure 1), but Kuhn et al. (2015b) incorrectly reported an older age for RCW 38. At that time, only 21 MYStIX young stars in RCW 38 had available Age_{JX} estimates; due to such a poor sampling, RCW 38 was omitted from further detailed age analyses by Getman et al.

Table 6
Age $_{JX}$ Stars in RCW 38

CXOU J	C_{net} (counts)	Age $_{JX}$ (Myr)
085820.49–473527.3	13.9	0.5
085821.18–473107.6	45.4	2.5
085831.44–472807.7	49.7	1.7
085834.11–472404.6	22.7	2.5
085835.29–472900.1	25.5	0.8
085840.64–473430.4	14.3	0.2
085841.56–472834.6	47.4	1.5
085849.32–473507.5	7.6	0.4
085850.80–473012.3	15.0	1.0
085853.52–472525.2	30.7	0.9
085853.96–472619.6	68.1	0.9
085854.97–472803.1	11.5	0.7
085857.56–472426.0	76.4	0.7
085859.82–473222.5	23.3	0.1
085859.89–473319.9	13.1	0.5
085859.96–473552.5	7.2	0.6
085859.98–472244.8	24.0	0.6
085901.48–473003.0	8.4	0.5
085903.76–472759.5	50.0	3.0
085910.52–472349.4	33.4	2.6
085923.68–473834.0	14.2	4.6
085924.71–473802.6	43.2	2.3
085924.98–473213.1	18.2	1.3
085927.72–473551.3	26.5	1.5
085927.86–472802.9	34.4	0.8
085931.28–473330.3	62.7	0.8
085935.41–473828.3	10.7	1.5
085935.52–473047.9	23.1	1.0
085937.73–473357.1	16.7	0.9
085940.23–473100.7	11.9	0.2
085942.68–472628.4	10.5	1.1
085944.48–473317.8	22.6	1.2
085948.39–472640.3	41.4	0.1
085949.65–473117.1	25.5	3.2
085957.85–473214.6	20.5	0.2
090006.73–473032.1	34.5	1.6

Note. Column 1: IAU designation. Column 2: X-ray net counts. Column 3: Age $_{JX}$ estimates.

We can now clarify this situation by combining the archive ~ 100 ks *Chandra* exposure of RCW 38 (obsid 2556) used in MYStIX with our new unpublished *Chandra* RCW 38 observations (obsids 16657, 17554, and 17681) with similar total exposure. Together, these observations yield a larger Age $_{JX}$ sample of 37 young stars with $> 7\text{--}10$ X-ray net counts. Because the near-IR photometry is prone to the effects of high absorption and diffuse nebular emission in the cluster core, all but one of the Age $_{JX}$ stars are located in the halo of the RCW 38 cluster. We thus are unable to evaluate whether a spatial age gradient is present (Getman et al. 2018a). The resulting stellar age estimates are listed in Table 6, and a histogram of the ages is presented in Figure 11. The median age for these 37 stars is 0.9 ± 0.1 Myr, and it is likely that the stars in the core are even younger. We conclude that the cluster RCW 38 has an age close to that of the IRAS 09002-4732 cluster, and both are unusually young among rich clusters in star-forming regions in the nearby Galactic Plane.

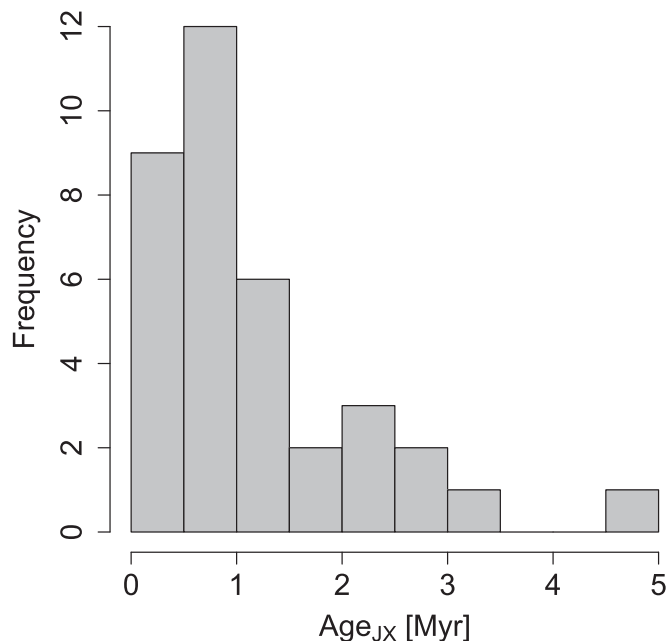


Figure 11. Histogram of stellar ages for the 37 young X-ray stars in RCW 38.

ORCID iDs

Konstantin V. Getman <https://orcid.org/0000-0002-6137-8280>

Eric D. Feigelson <https://orcid.org/0000-0002-5077-6734>

Michael A. Kuhn <https://orcid.org/0000-0002-0631-7514>

Patrick S. Broos <https://orcid.org/0000-0002-7872-2025>

Gordon P. Garmire <https://orcid.org/0000-0002-7371-5416>

References

- Allen, C., Costero, R., Ruelas-Mayorga, A., et al. 2017, *MNRAS*, **466**, 4937
- André, P., Men'shchikov, A., Bontemps, S., et al. 2010, *A&A*, **518**, L102
- Apai, D., Linz, H., Henning, T., & Stecklum, B. 2005, *A&A*, **434**, 987
- Baddeley, A., Rubak, E., & Turner, R. 2015, *Spatial Point Patterns: Methodology and Applications with R* (Boca Raton, FL: CRC Press)
- Bally, J. 2008, in *Handbook of Star-forming Regions, Vol. I The Northern Sky*, ed. B. Reipurth (San Francisco, CA: ASP), 459
- Bally, J., Langer, W. D., Stark, A. A., et al. 1987, *ApJL*, **312**, L45
- Bate, M. R., Bonnell, I. A., & Bromm, V. 2003, *MNRAS*, **339**, 577
- Bik, A., Lenorzer, A., Kaper, L., et al. 2003, *A&A*, **404**, 249
- Bik, A., Stolte, A., Gennaro, M., et al. 2014, *A&A*, **561**, A12
- Blaauw, A. 1991, in *The Physics of Star Formation and Early Stellar Evolution*, Vol. 342, ed. C. J. Lada & N. D. Kylafis (Dordrecht: Kluwer), 125
- Bouy, H., Alves, J., Bertin, E., Sarro, L. M., & Barrado, D. 2014, *A&A*, **564**, A29
- Broos, P. S., Getman, K. V., Povich, M. S., et al. 2013, *ApJS*, **209**, 32
- Broos, P. S., Townsley, L. K., Feigelson, E. D., et al. 2010, *ApJ*, **714**, 1582
- Carpenter, J. M., Hillenbrand, L. A., & Skrutskie, M. F. 2001, *AJ*, **121**, 3160
- Chandra X-ray Center 2018, *The Chandra Proposers' Observatory Guide*, version 21.0, <http://asc.harvard.edu/proposer/POG>
- Cyganowski, C. J., Whitney, B. L., Holden, E., et al. 2008, *AJ*, **136**, 2391
- DeRose, K. L., Bourke, T. L., Gutermuth, R. A., et al. 2009, *AJ*, **138**, 33
- Elmgreen, B. G. 2000, *ApJ*, **530**, 277
- Federrath, C. 2015, *MNRAS*, **450**, 4035
- Feigelson, E. D. 2018, in *The Birth of Star Clusters*, Vol. 424, ed. S. Stahler (Cham: Springer), 119
- Feigelson, E. D., Getman, K., Townsley, L., et al. 2005, *ApJS*, **160**, 379
- Feigelson, E. D., & Townsley, L. K. 2008, *ApJ*, **673**, 354
- Feigelson, E. D., Townsley, L. K., Broos, P. S., et al. 2013, *ApJS*, **209**, 26
- Gaia Collaboration, Brown, A. G. A., Vallenari, A., et al. 2018, *A&A*, **616**, A1
- Gaia Collaboration, Prusti, T., et al. 2016, *A&A*, **595**, A1
- Garmire, G. P., Bautz, M. W., Ford, P. G., Nousek, J. A., & Ricker, G. R., Jr. 2003, *Proc. SPIE*, **4851**, 28
- Getman, K. V., Broos, P. S., Kuhn, M. A., et al. 2017, *ApJS*, **229**, 28
- Getman, K. V., Feigelson, E. D., Broos, P. S., Townsley, L. K., & Garmire, G. P. 2010, *ApJ*, **708**, 176
- Getman, K. V., Feigelson, E. D., Kuhn, M. A., et al. 2014, *ApJ*, **787**, 108
- Getman, K. V., Feigelson, E. D., Kuhn, M. A., et al. 2018a, *MNRAS*, **476**, 1213
- Getman, K. V., Feigelson, E. D., Kuhn, M. A., et al. 2019, *MNRAS*, **487**, 2977
- Getman, K. V., Flaccomio, E., Broos, P. S., et al. 2005, *ApJS*, **160**, 319
- Getman, K. V., Kuhn, M. A., Feigelson, E. D., et al. 2018b, *MNRAS*, **477**, 298
- Ghosh, S. K., Mookerjee, B., Rengarajan, T. N., Tandon, S. N., & Verma, R. P. 2000, *A&A*, **363**, 744
- Grosso, N., Feigelson, E. D., Getman, K. V., et al. 2005, *ApJS*, **160**, 530
- Güdel, M. 2007, *LRSF*, **4**, 3
- Hillenbrand, L. A. 1997, *AJ*, **113**, 1733
- Johnstone, D., & Bally, J. 1999, *ApJL*, **510**, L49
- Johnstone, D., Ciccone, S., Kirk, H., et al. 2017, *ApJ*, **836**, 132
- Kim, H.-J., Koo, B.-C., & Davis, C. J. 2015, *ApJ*, **802**, 59
- Kounkel, M., Covey, K., Suárez, G., et al. 2018, *AJ*, **156**, 84
- Kroupa, P. 2001, *MNRAS*, **322**, 231
- Krumholz, M. R., & McKee, C. F. 2019, arXiv:1909.01565
- Krumholz, M. R., McKee, C. F., & Bland-Hawthorn, J. 2019, *ARA&A*, **57**, 227
- Kuhn, M. A., & Feigelson, E. D. 2019, arXiv:1711.11101
- Kuhn, M. A., Feigelson, E. D., Getman, K. V., et al. 2014, *ApJ*, **787**, 107
- Kuhn, M. A., Feigelson, E. D., Getman, K. V., et al. 2015a, *ApJ*, **812**, 131
- Kuhn, M. A., Getman, K. V., Broos, P. S., et al. 2013, *ApJS*, **209**, 27
- Kuhn, M. A., Getman, K. V., & Feigelson, E. D. 2015b, *ApJ*, **802**, 60
- Kuhn, M. A., Getman, K. V., Feigelson, E. D., et al. 2017, *AJ*, **154**, 214
- Kuhn, M. A., Hillenbrand, L. A., Sills, A., et al. 2019, *ApJ*, **870**, 32
- Kusune, T., Sugitani, K., Nakamura, F., et al. 2016, *ApJL*, **830**, L23
- Lada, C. J., & Lada, E. A. 2003, *ARA&A*, **41**, 57
- Lapinov, A. V., Schilke, P., Juvela, M., & Zinchenko, I. I. 1998, *A&A*, **336**, 1007
- Lenzen, R. 1991, *A&A*, **244**, 477
- Mac Low, M.-M., & Klessen, R. S. 2004, *RvMP*, **76**, 125
- Megeath, S. T., Gutermuth, R., Muzerolle, J., et al. 2012, *AJ*, **144**, 192
- Moriguchi, Y., Yamaguchi, N., Onishi, T., et al. 2001, *PASJ*, **53**, 1025
- Mottram, J. C., Hoare, M. G., Lumsden, S. L., et al. 2007, *A&A*, **476**, 1019
- Naylor, T., Broos, P. S., & Feigelson, E. D. 2013, *ApJS*, **209**, 30
- O'Dell, C. R. 2001, *ARA&A*, **39**, 99
- O'Dell, C. R., Henney, W. J., Abel, N. P., et al. 2009, *AJ*, **137**, 367
- Palla, F., & Stahler, S. W. 2000, *ApJ*, **540**, 255
- Pflamm-Altenburg, J., & Kroupa, P. 2006, *MNRAS*, **373**, 295
- Popescu, B., & Hanson, M. M. 2014, *ApJ*, **780**, 27
- Povich, M. S., Kuhn, M. A., Getman, K. V., et al. 2013, *ApJS*, **209**, 31
- Povich, M. S., Townsley, L. K., Robitaille, T. P., et al. 2016, *ApJ*, **825**, 125
- Rezaei, Kh. S., Bailer-Jones, C. A. L., Schlafly, E. F., & Fouesneau, M. 2018, *A&A*, **616**, A44
- Richert, A. J. W., Getman, K. V., Feigelson, E. D., et al. 2018, *MNRAS*, **477**, 5191
- Rivera-Ingraham, A., Martin, P. G., Polychroni, D., et al. 2013, *ApJ*, **766**, 85
- Rodney, S. A., & Reipurth, B. 2008, in *Handbook of Star-forming Regions, Vol. II*, ed. B. Reipurth (San Francisco, CA: ASP), 683
- Romine, G., Feigelson, E. D., Getman, K. V., Kuhn, M. A., & Povich, M. S. 2016, *ApJ*, **833**, 193
- Schneider, N., Csengeri, T., Bontemps, S., et al. 2010, *A&A*, **520**, A49
- Siess, L., Dufour, E., & Forestini, M. 2000, *A&A*, **358**, 593
- Stelzer, B., Flaccomio, E., Montmerle, T., et al. 2005, *ApJS*, **160**, 557
- Teixeira, P. S., Lada, C. J., Young, E. T., et al. 2006, *ApJL*, **636**, L45
- Tieftrunk, A. R., Gaume, R. A., Claussen, M. J., et al. 1997, *A&A*, **318**, 931
- Tieftrunk, A. R., Gaume, R. A., & Wilson, T. L. 1998, *A&A*, **340**, 232
- Townsley, L. K., Broos, P. S., Chu, Y.-H., et al. 2011a, *ApJS*, **194**, 15
- Townsley, L. K., Broos, P. S., Corcoran, M. F., et al. 2011b, *ApJS*, **194**, 1
- Uchida, Y., Fukui, Y., Minoshima, Y., et al. 1991, *Natur*, **349**, 140
- Vázquez-Semadeni, E., González-Samaniego, A., & Colín, P. 2017, *MNRAS*, **467**, 1313
- Vázquez-Semadeni, E., Palau, A., Ballesteros-Paredes, J., Gómez, G. C., & Zamora-Avilés, M. 2019, *MNRAS*, **490**, 3061
- Wang, K., Zhang, Q., Testi, L., et al. 2014, *MNRAS*, **439**, 3275
- Wang, L., Kroupa, P., & Jerabkova, T. 2019, *MNRAS*, **484**, 1843
- Wilms, J., Allen, A., & McCray, R. 2000, *ApJ*, **542**, 914
- Wolk, S. J., Bourke, T. L., & Vigil, M. 2008, in *Handbook of Star-forming Regions, Vol. II*, ed. B. Reipurth (San Francisco, CA: ASP), 124
- Wood, D. O. S., & Churchwell, E. 1989, *ApJS*, **69**, 831
- Yamaguchi, N., Mizuno, N., Saito, H., et al. 1999, *PASJ*, **51**, 775
- Zhang, C.-P., Yuan, J.-H., Li, G.-X., Zhou, J.-J., & Wang, J.-J. 2017, *A&A*, **598**, A76
- Zhu, H., Tian, W., Li, A., & Zhang, M. 2017, *MNRAS*, **471**, 3494